Research Square

Preprints are preliminary reports that have not undergone peer review.
They should not be considered conclusive, used to inform clinical practice,
or referenced by the media as validated information.

Targeting the inflamed paraventricular hypothalamic-bone marrow axis rejuvenates lymphopoiesis in aged mice

Wei-Na Jin

weina.jin@ncrcnd.org.cn

Capital Medical University https://orcid.org/0000-0002-2196-9078

Meng Jia

Beijing Tiantan Hospital, Capital Medical University

Shihe Jiang

Beijing Tiantan Hospital, Capital Medical University

Yiyuan Xu

Beijing Tiantan Hospital, Capital Medical University

Tian Lan

Beijing Tiantan Hospital, Capital Medical University

Haonan Guan

Beijing Tiantan Hospital, Capital Medical University

Yingying Chang

Tianjin Medical University General Hospital

Zhilin Chang

https://orcid.org/0000-0003-3982-6240

Zhongpeng Zhao

State Key Laboratory of Pathogens and Biosecurity https://orcid.org/0000-0002-9147-6252

Wenyan He

Beijing Tiantan Hospital, Capital Medical University https://orcid.org/0000-0002-8752-4768

Kaibin Shi

Department of Neurology, China National Clinical Research Center for Neurological Diseases, Beijing Tiantan Hospital, Capital Medical University

Sara Palma-Tortosa

Laboratory of Stem Cells and Restorative Neurology, Lund Stem Cell Center, Lund University
https://orcid.org/0000-0002-0648-8380

Zaal Kokaia

Laboratory of Stem Cells and Restorative Neurology, Lund Stem Cell Center, Lund University
https://orcid.org/0000-0003-2296-2449

Gerry Melino
University of Rome Tor Vergata https://orcid.org/0000-0001-9428-5972
Hans-Gustaf Ljunggren
Karolinska Institute https://orcid.org/0000-0003-0908-7387
Luc Van Kaer
Department of Pathology, Microbiology and Immunology, Vanderbilt University Medical Center, Nashville, TN, USA. https://orcid.org/0000-0001-5275-2309
Fu-Dong Shi
Beijing Tiantan Hospital, Capital Medical University https://orcid.org/0000-0002-9675-4637

Article

Keywords: Aging, neuroimmune interaction, paraventricular nucleus (PVN), Toll like receptor 4 (TLR4), lymphopoiesis

Posted Date: November 2nd, 2026

DOI: https://doi.org/10.21203/rs.3.rs-9350529/v1

License: This work is licensed under a Creative Commons Attribution 4.0 International License.
Read Full License

Additional Declarations: There is **NO** Competing Interest.

Targeting the inflamed paraventricular hypothalamic-bone marrow axis rejuvenates lymphopoiesis in aged mice

Meng Jia[1#], Shihe Jiang[1#], Yiyuan Xu[1], Tian Lan[1], Haonan Guan[1], Yingying Chang[2], Zhilin Chang[1], Zhongpeng Zhao[3], Wenyan He[1], Kaibin Shi[1], Sara Palma-Tortosa[4], Zaal Kokaia[4], Gerry Melino[5], Hans-Gustaf Ljunggren[6], Luc Van Kaer[7], Fu-Dong Shi[1,2], Wei-Na Jin[1*]

[1] Department of Neurology, China National Clinical Research Center for Neurological Diseases, Beijing Tiantan Hospital, Capital Medical University, Beijing, 100070, China.

[2] Department of Neurology, Tianjin Medical University General Hospital, Tianjin, 300052, China.

[3] Cheeloo College of Medicine, Shandong University, Jinan, 250012, China.

[4] Laboratory of Stem Cells and Restorative Neurology, Lund Stem Cell Center, Lund University, 22184 Lund, Sweden.

[5] Department of Experimental Medicine, TOR, University of Rome Tor Vergata, Rome 00133, Italy.

[6] Center for Infectious Medicine, Department of Medicine Huddinge, Karolinska Institute, Karolinska University Hospital, Stockholm, 17176, Sweden.

[7] Department of Pathology, Microbiology, and Immunology, Vanderbilt University School of Medicine, Nashville, TN 37232, USA.

[#]Dr. Jia and Dr. Jiang contributed equally to this work.

*Correspondence should be addressed to Wei-Na Jin, weina.jin@ncrcnd.org.cn.

Summary

Older individuals are prone to infectious disease, cancer and exhibit reduced vaccine efficacy due to age-associated immune dysfunction. The immune and nervous systems are anatomically and functionally connected, and brain aging contributes to the development of neurodegenerative disorders, including Parkinson's and Alzheimer's diseases. However, how the aging brain contributes to age-associated immune dysfunction, and which organ systems are involved, remains poorly understood. Here, we show that bone marrow from elderly humans and mice displays a reduced frequency and aberrant transcriptomes of common lymphoid progenitors (CLPs), accompanied by impaired lymphopoiesis. Neural denervation preserved lymphopoiesis and CLP abundance, indicating neural regulation of the bone marrow. Retrograde tracing from the bone marrow identified corticotropin-releasing hormone-expressing neurons in the paraventricular nucleus (PVN-CRH neurons) as a major participant in controlling lymphoid output. Mechanistically, aging triggers Toll-like receptor 4 (TLR4)–interferon signaling in PVN-CRH neurons, eliciting inflammatory hyperactivation. This hyperactivity destabilized DNA nucleotidylexotransferase (TdT/DNTT) expression in hematopoietic stem and progenitor cells (HSPCs) and disrupted lymphoid developmental trajectories in bone marrow via sympathetic output-β adrenergic receptors signal. Chemogenetic inhibition of aged PVN-CRH neurons or CRH neuron-specific TLR4 ablation restored CLPs and B-cell production in bone marrow and improved the H1N1 vaccine response in aged mice. In conclusion, our findings reveal a brain–bone marrow axis that becomes dysregulated with aging and propose neuromodulation as a potential strategy to rejuvenate immune function in older individuals.

Key words: Aging, neuroimmune interaction, paraventricular nucleus (PVN), Toll like receptor 4 (TLR4), lymphopoiesis.

Introduction

Aging poses significant global challenges to health, society, and the economy[1,2]. As a critical guardian of external and internal threats, the immune system is particularly affected by aging, resulting in increased susceptibility to infections, cancer, and reduced vaccine efficacy[3-7]. The immune and central nervous systems (CNS) are anatomically and functionally interconnected[8-10]: Immune invasion of the CNS can precipitate inflammatory diseases such as multiple sclerosis; Conversely, acute brain injuries including stroke and traumatic brain injury can profound dynamic alterations in systemic immune responses[8, 11]. While current understanding has been gained from studies on acute stress and inflammation, the specific neural pathways and mechanisms through which normal brain aging influences the decline of immune competency are still not fully comprehended.

Current understanding of neural regulation of the immune system highlights two principal pathways: central control through hypothalamic-pituitary-adrenal (HPA) axis signaling[12-14], and peripheral innervation via sympathetic and nociceptive nerves that modulate hematopoiesis in the bone marrow[15-17]. Aging disrupts this balance although previous findings have been conflicting. For example, Ho et al. reported an increase in tyrosine hydroxylase-positive (TH^+) sympathetic nerves in aged bone marrow, leading to myeloid expansion[15]; whereas Maryanovich et al. demonstrated that aging results in the loss of niche-associated adrenergic nerves, thereby impairing hematopoietic stem cell (HSC) maintenance[16]. Critically, it remains unknown whether and how neural circuits from the aging CNS influence bone marrow function and immune output. To bridge this gap, by combining human bone marrow scRNA-transcriptomes/Olink proteomics, mice long-range retrograde tracing, whole-brain 3D imaging, and spatial transcriptomics, we identified a neuroimmune pathway connecting hypothalamic PVN-CRH neurons to the bone marrow, crucial for maintaining lymphopoiesis. In aging brain, neuronal hyperactivation through TLR4-IFNγ signaling, disrupts lymphoid output and immune competence. These findings establish a brain–bone marrow axis as a key player in age-associated immune dysfunction and highlight the therapeutic potential of targeting the hypothalamic PVN to rejuvenate immune function in aging.

Results

Aberrant bone marrow lymphopoiesis in aged humans and mice

To investigate aging bone marrow composition and transcriptomic characteristics, we recruited healthy individuals over 60 years of age and under 40 years of age for detailed analysis (**Figure 1A, Supplementary Figure 1A**). As an initial validation, we confirmed that aged individuals exhibit increased frequencies of neutrophils and reduced lymphocytes in peripheral blood compared with younger subjects (**Figure 1B**). To examine bone marrow composition, where these cells originate, we performed high-resolution clustering of hematopoietic stem and progenitor cells (HSPCs) identifying hematopoietic stem cells (HSCs), multipotent progenitors (MPPs), lymphoid-primed multipotent progenitors (LMPPs), proliferating LMPPs (LMPP_TK1), common lymphoid progenitors (CLPs), and granulocyte-monocyte progenitors (GMPs) **(Fig. 1C, Supplementary Figure 1B)**. We observed a reduced frequency of MPPs (27% to 15%) and an increased frequency of LMPPs (21% to 35%) in aged individuals, suggesting accelerated differentiation

dynamics. In addition, CLP frequency was reduced from 11% to 7% **(Figure 1C)**, indicating impaired lymphoid output and a shift toward myeloid-biased hematopoiesis. Reduced lymphoid scores across aged HSPC subsets further supported this bias **(Figure. 1D, Supplementary Figure 1C)**.

Several genes involved in lymphopoiesis, including DNA nucleotidylexotransferase (DNTT), were significantly decreased within the CLP cluster (**Figure 1E**). Given the established role of DNTT in early B-lineage development, its reduced expression suggests impaired B cell lymphopoiesis in aged bone marrow. Notable, the frequency of LMPP_TK1, a T and natural killer (NK) cell-biased progenitor, was unchanged, suggesting that the observed reduction in lymphocytes primarily reflects impaired B cell lymphopoiesis. Consistent with this interpretation, pseudotime analysis detected a development lineage from HSCs to naïve_B cells and confirmed impaired B cell lymphopoiesis in bone marrow of aged humans (**Figure 1F, G, Supplementary Figure 1D**). Further clustering of the B-cell lineage revealed that early developmental stages, including mitotic B-cells and pro-B cells, were markedly reduced in aged bone marrow (**Figure 1H, Supplementary Figure 1E**). Secretome analysis further revealed downregulation of multiple secretory factors, including PADI2, BACH1, HEXIM1, and upregulation of immune inhibitory receptor KLRD1 compared with young controls, consistent with impaired lymphopoiesis and altered bone marrow signaling **(Figure 1I)**.

We next examined whether comparable alterations occur in mice. Single-cell RNA sequencing of bone marrows from 3-month-old and 18-month-old mice revealed cellular clustering and transcriptomic features similar to those observed in humans (**Figure 1J-L, Supplementary Figure 2A-D**). Flow cytometry analysis further showed reduced CLPs and total B cells in bone marrow of 18-month-old mice, whereas HSCs, GMPs, CMPs, T cells, and NK cells were significantly increased (**Figure 1M, Supplementary Figure 2E**). Together, these findings indicate that both aged humans and mice share a conserved aging phenotype characterized by impaired lymphopoiesis and reduced B-lineage development.

The paraventricular nucleus (PVN) neurons exhibit hyperactivity in aged mice

The central nervous system (CNS), through neuroendocrine signaling and neural connection, has long been recognized as a regulator of immune reactivity in peripheral organs[9, 10, 16, 18]. To determine whether the aging CNS influences lymphopoiesis within the bone marrow, we performed unilateral femoral nerve denervation in 18-month-old mice. This intervention corrects the myeloid bias toward lymphopoiesis without influencing HSC self-renewal, resulting in increased CLP abundance (**Figure 2A**).

To identify the specific brain region involved in this regulatory circuit, we performed retrograde tracing by injecting pseudorabies virus (PRV) into the unilateral femoral bone marrow (**Supplementary Figure 3A-C**). Whole-brain three-dimensional imaging using fluorescence micro-optical sectioning tomography (fMOST) revealed PRV-labeled neurons in several regions, including the paraventricular nucleus (PVN) of the hypothalamus, basolateral amygdala (BLA), the Motor cortex 1, and nucleus tractus solitarius (NTS) (**Figure 2B**). Quantitative analysis showed that 18-month-old mice exhibited increased numbers of $EGFP^+$ neurons in the PVN and NTS but

fewer labeled neurons in the M1 and BLA compared with 3-month-old mice (**Figure 2B**). Tyrosine hydroxylase (TH) staining of sympathetic ganglia confirmed that bone marrow innervating fibers were sympathetic in origin (**Supplementary Figure 3B**).

The c-Fos staining of these nuclei showed that c-Fos$^+$ neurons were only increased in the PVN of 18-month-old mice, indicating its specifical role in mediating dysfunction of brain-bone marrow axis in 18-month-old mice (**Figure 2C, Supplementary Figure 3D, E**). Moreover, the PVN is well known for its central role in regulating peripheral immune responses[18-20]. Morphological analysis revealed that EGFP$^+$ neurons in the PVN of 18-month-old mice displayed larger volume than those in 3-month-old mice (**Supplementary Figure 3F, G**). Calcium signal recording confirmed that PVN neurons from 18-month-old mice exhibited higher calcium signaling activity compared with those from 3-month-old mice (**Figure 2D, E, Supplementary Figure 4H**).

To further investigate age-associated neuronal changes in the PVN, we employed designer receptors exclusively activated by designer drugs (DREADDs) to either activate or inhibit PVN neurons and then examined HSPCs in the bone marrow (**Supplementary Figure 4A-C**). Activation of PVN neurons in 3-month-old mice reduced CLPs and total B-cells, recapitulating the aged phenotype. Conversely, inhibition of PVN neurons in 18-month-old mice increased CLPs, with no significant effect in 3-month-old controls (**Supplementary Figure 4D-G**). Together, these findings identify a neural circuit from the PVN to bone marrow that regulates B cell lymphopoiesis, and that becomes dysregulated during aging.

PVN-CRH neurons regulate B cell lymphopoiesis in bone marrow of aged mice

Following confirmation that the retrogradely labeled neurons were Corticotropin-releasing hormone (CRH)-positive (**Figure 2F**), we used a CRH promoter-driven DREADD viral system to selectively manipulate the activity of these neurons (**Figure 2G**, **Supplementary Figure 5A**). Inhibition of CRH neurons using the inhibitory DREADD receptor hM4Di reduced c-Fos expression in the PVN of 18-month-old mice (**Figure 2H**), confirming effective neuronal silencing. In 18-month-old mice, administration of the DREADD ligand clozapine-N-oxide (CNO) resulted in a rapid increase in CLPs within bone marrow (**Figure 2I**). This effect propagated through the B cell lymphopoiesis cascade, leading to significant increases in early pro-B, pre-B, and immature B cells, as well as total B-cell numbers at 14 days after treatment, without altering the HSC pool (**Figure 2I**). These results indicate that suppressing hyperactivity PVN-CRH neurons restores B cell lymphopoiesis in bone marrow of 18-month-old mice. Conversely, DREADD-mediated activation of PVN-CRH neurons (hM3Dq) in 3-month-old mice suppressed early B cell lymphopoiesis (early pro-B and pre-B cells) and reduced HSC self-renewal capacity, recapitulating the defects observed during natural aging (**Supplementary Figure 5A-D, F**).

With these findings in hand, we next sought to distinguish between neural and humoral mechanisms underlying PVN-mediated immune regulation. To this end, we performed unilateral femoral nerve denervation followed by chemogenetic inhibition of PVN neurons in 18-month-old mice (**Supplementary Figure 5E**). Flow cytometry analysis showed that denervation on the ipsilateral side completely abolished the pro-lymphopoietic effects of PVN inhibition, specifically affecting CLPs, pre-pro-B, and early pro-B cells, while leaving HSCs unaffected (**Figure 2J**).

These results demonstrate that PVN neurons regulate bone marrow B cell lymphopoiesis through neural activity within the PVN-bone marrow sympathetic circuit, rather than through systemic hormonal signaling.

Aging activates bone marrow-regulating PVN-CRH neurons through TLR4-IFNγ signaling

To investigate why PVN-CRH neurons become hyperactive in 18-month-old mice, we performed spatial transcriptomic profiling (digital spatial profiling, DSP), specifically targeting $EGFP^+$ PVN neurons following retrograde tracing (**Figure 3A-C, Supplementary Figure 6**). This analysis revealed robust activation of TLR4 signaling in bone marrow-tracing neurons within the PVN of 18-month-old mice (**Figure 3B**). Consistent with this observation, expression of genes associated with neuronal activity and inflammation, including *Il1b*, *Ifng*, *Cxcl10*, and *Junb*, were elevated in the PVN of 18-month-old mice (**Figure 3C**). Co-staining for CRH and TLR4 further demonstrated increased TLR4 expression in CRH neurons (**Figure 3D**). This age-associated increase in TLR4 expression was further validated at the ultrastructural level using immunoelectron microscopy (**Figure 3E**).

TLR4-bearing microglia could potentially contribute to the regulation of PVN neuronal activity. To investigate this possibility, we established an *in vitro* neuronal senescence model using primary hypothalamic neurons cultured for an extended period (21 days *in vitro*, DIV 21) (**Figure 3F**). In this model, mRNA levels of *Tlr4* and *Il1b* were elevated at DIV 21, whereas *Ifng* expression increased earlier at DIV 14 (**Figure 3F**). Protein levels of TLR4 and IFNγ, together with downstream signaling components phosphorylated NF-κB and IκB, were also increased at DIV 21, indicating activation of the TLR4 pathway during neuronal senescence (**Figure 3G**). These findings were consistent with the spatial transcriptomic results observed *in vivo*. In parallel, the proportion of c-Fos^+ neurons increased significantly at DIV 21 (**Figure 3H**), coinciding with the appearance of the senescence marker β-galactosidase (β-gal) (**Figure 3I**). These observations suggest that the neuronal senescence model recapitulates the key features of PVN neurons in aged mice. Notably, hypothalamic neurons developed an inflammatory activation phenotype during senescence even in the absence of other resident immune cells, particularly microglia.

To further examine role of TLR4-driven hyperactivation of PVN-CRH neurons during aging, we delivered a CRH neuron-specific TLR4-knockdown AAV into the PVN of 18-month-old mice (**Figure 3J**). TLR4 expression was markedly reduced in CRH neurons in the shRNA (Tlr4) group (**Figure 3J**). Consistently with this intervention, hyperactivity of CRH neurons in the PVN of 18-month-old mice was significantly reduced following TLR4 knockdown (**Figure 3K**). Collectively, these findings indicate that aging activates neuronal TLR4 signaling to activate PVN-bone marrow axis in 18-month-old mice.

DNTT mediates neural modulation of B cell lymphopoiesis during aging

To investigate the intracellular mechanism in HSPCs that mediates neural-regulation of B cell lymphopoiesis, we isolated HSCs (Lin^-c-$Kit^+Sca1^+CD48^-CD150^+$) from bone marrow following DREADD-mediated inhibition of PVN-CRH neurons in 18-month-old mice (**Figure 4A-C, Supplementary Figure 5G**). RNA sequencing revealed enrichment of transcripts associated with

cellular differentiation and neuroactive ligand–receptor signaling pathways in HSCs after PVN-CRH neuron inhibition (**Figure 4D**), suggesting enhanced interaction between HSCs and neural signals within the bone marrow microenvironment. Among the neural PVN-CRH neuron–regulated differentially expressed genes (DEGs), DNA nucleotidylexotransferase (DNTT) expression increased nearly fourfold compared with controls (**Figure 4B**). DNTT is a key regulator of B cell lymphopoiesis and maturation and was markedly reduced in CLP cluster of both aged humans and 18-month-old mice (**Figure 1E, K**). Moreover, DNTT protein levels were inversely correlated with CRH neuronal activity in the PVN (**Figure 4E**), suggesting that DNTT mediates neural activity-dependent regulation of bone marrow B cell lymphopoiesis during aging.

To further investigate the role of DNTT in age associated lymphopoiesis impairment, we established an *in vitro* differentiation system in which LSK cells (Lineage$^-$Sca-1$^+$c-Kit$^+$) sorted from 3-month-old and 18-month-old mice were induced toward CLP development (**Figure 4F**, **Supplementary Figure 5G, 7A**). Using this model, we observed a marked reduction in DNTT expression in LSK and CLP cells of 18-month-old mice, which was restored upon induction of differentiation toward CLPs (**Figure 4G, Supplementary Figure 7B**). We next manipulated DNTT levels using lentiviral vectors for knockdown or overexpression (**Supplementary Figure 7C, D**). Knockdown of DNTT in LSK cells of 3-month-old mice reduced the proportion of CLPs and suppressed expression of PAX5, which was essential for B cell lymphopoiesis (**Figure 4H**). Whereas DNTT overexpression in LSK cells of 18-month-old mice increased CLP generation (**Figure 4I**), supporting a role for DNTT in promoting CLP differentiation. Consistent with neural regulation of this process, co-localization of PRV-EGFP$^+$ neurons with the noradrenergic marker TH was observed in sympathetic ganglion (**Supplementary Figure 3B**). β2/3-adrenoceptor staining of sorted LSK cells confirms that HSPCs in bone marrow expresses β-adrenoceptor[16, 21, 22]. Treatment of LSK cells with β-adrenoceptor antagonist propranolol impaired CLP differentiation (**Figure 4K, Supplementary Figure 7E**). Together, these findings indicate that reduced DNTT expression contributes to impaired CLP differentiation in LSK cells of 18-month-old mice, and that DNTT-dependent lymphopoiesis is modulated by sympathetic neural signaling.

Inhibiting neural hyperactivity improves vaccine efficacy in aged mice

Vaccine efficacy declines markedly in older individuals[23], impaired B-cell immunity is a major contributing factor in the aged population[24-26]. To investigate whether neural modulation affects immune responses during aging, we established an H1N1 vaccination model in mice (**Figure 5A, B**). Inhibition of PVN-CRH neurons using CRH specific DREADD in 18-month-old mice significantly increased activated B cells (CD69$^+$) and enhanced H1N1 antibody production (**Figure 5C, D**). Conversely, activation of PVN-CRH neurons in 3-month-old mice suppressed B cell lymphopoiesis and reduced antibody production (**Figure 5E**). These results suggest that suppressing neural hyperactivity can improve vaccine-induced immune responses in 18-month-old mice.

We further examined the role of TLR4 driven hyperactivation of PVN-CRH neurons in vaccine-induced immune responses in 18-month-old mice. Blocking TLR4 in PVN-CRH neurons reversed

age-associated defects in B-cell activation and enhanced H1N1 antibody production in 18-month-old mice (**Figure 5F, G**). Improved B cell lymphopoiesis was accompanied by increased DNTT expression in both HSCs and CLPs (**Figure 5H, I**), indicating that TLR4 inhibition promotes B cell lymphopoiesis through DNTT-dependent mechanisms. Together, these findings suggest that targeting neuronal TLR4 signaling may represent a promising strategy to restore vaccine responsiveness during aging.

Discussion

This study identifies PVN-CRH neurons participating in a neural circuit through which PVN-originated signals reach the bone marrow via the sympathetic nervous system, thus modulating bone marrow lymphopoiesis. During aging, these PVN-CRH neurons enter a hyperactivation state triggered by TLR4-interferon signaling. This hyperactivation disrupts the bone marrow niche and impairs B cell lymphopoiesis by destabilizing TdT/DNTT expression in hematopoietic stem and progenitor cells. Inhibiting these overexcited PVN neurons restored B cell lymphopoiesis and improved the immune response to vaccination in the aged mice. Collectively, our findings reveal that a PVN-to-bone marrow neural circuit, distinct from classical neuroendocrine mechanisms, regulates lymphopoiesis and effective immune responses during aging.

Cellular senescence and the associated senescence-associated secretory phenotype (SASP) have traditionally been described in proliferating cells and are known to contribute to tissue aging and chronic inflammation[27]. Our findings suggest that post-mitotic neurons can also adopt a functionally detrimental state. We observed increased numbers of c-Fos$^+$ and higher calcium signaling of PVN-CRH neurons in 18-month-old mice, indicating elevated neural activity[28,29]. The hyperactivation of PVN-CRH neurons, characterized by increased *Il1b*, *Ifng*, and *Cxcl10* expression, mirrors key features of the SASP. This observation aligns with the emerging concept of "neuronal senescence", in which neurons exhibit reduced plasticity, metabolic stress, and pro-inflammatory signaling, potentially acting as reservoirs of age-associated inflammation[30,31].

Although TLR4-mediated neuroinflammation has been extensively characterized in glial cells[32-34], our results suggest that hypothalamic neurons themselves can harness TLR4 signaling to exert remote and profound effects on bone marrow, the primary site of immune cell generation. Consistent with this idea, previous studies have shown that aging mobilizes CRH neurons in the PVN, with increased neuronal number and co-expression with Arginine Vasopressin (AVP) in the human hypothalamus[35-37]. Moreover, Cai et al. reported chronic activation of the IKKβ/NF-κB pathway in the hypothalamus during aging, and inhibition of this pathway slowed aging progression[38]. Functional neuroimaging studies further support this concept: resting-state fMRI analyses have demonstrated increased fractional amplitude of low-frequency fluctuations (fALFF) in the thalamus of older individuals, suggesting elevated neural activity in aging brains[39].

How bone marrow hematopoiesis responds to neural regulation, particularly during aging, remains poorly understood. We identified downregulation *of Dntt* RNA in CLPs from both aged humans and mice. DNTT, also known as terminal deoxynucleotidyl transferase (TdT), is a key enzyme required for early B cell lymphopoiesis and V(D)J recombination during B cell maturation[40-42]. RNA sequencing revealed that DREADD-mediated inhibition of PVN-CRH neurons

increased *Dntt* expression by approximately fourfold in HSCs and promoted differentiation toward CLPs. Consistent with this observation, flow cytometric analysis showed that the proportion of $DNTT^{high}$ HSCs in bone marrow was inversely correlated with the activity of PVN-CRH neurons in the PVN. These findings indicate that excessive PVN-bone marrow neural circuit suppresses B cell lymphopoiesis during aging by reducing DNTT expression. Restoration of DNTT function in aged HSCs may therefore help re-establish hematopoietic homeostasis and enhance B-cell-dependent humoral immunity.

The identification of a neural circuit controlling lymphopoiesis suggests new therapeutic opportunities to enhance immune function by targeting the brain. For example, senolytic therapies, may help eliminate dysfunctional neuronal populations restore the activity of PVN-CRH neurons, thereby improving lymphoid output. In addition, neuromodulation strategies, including non-invasive stimulation of hypothalamic circuits, may suppress hyperactive PVN-CRH-bone marrow signaling and represent a potential strategy to restore immune function.

This study has several limitations. The number of human samples analyzed was relatively small. Furthermore, the chemogenetic manipulations on PVN-CRH neurons could not exclude indirect neuroendocrine mechanisms. Additionally, although we used AAV-mediated TLR4 knockdown to interrogate neuronal signaling pathways, we did not evaluate genetic models of physiological aging. Future studies incorporating these approaches will help further clarify the contribution of this neuronal contribution to age-associated immune dysfunction. Despite these limitations, this work emphasizes PVN-CRH neurons as active contributor of systemic immune aging, proposing neuromodulation as a promising strategy for revitalizing immune function in the elderly.

Acknowledgements

We thank all bone marrow donors for their contributions to this study. This work was supported in part by the National Natural Science Foundation of China (82401580), the Beijing Natural Science Foundation (JQ26041), and Fundamental and Interdisciplinary Disciplines Breakthrough Plan of the Ministry of Education of China (JYB2025XDXM603).

Author Contributions

W.-N.J. formulated the study concept. M.J., S.J., Y.X., T.L., H.G., and Y.C. performed the experiments. W.-N.J., Z.C., Z.Z., K.S., S.P.-T. and W.H. analyzed the data and interpreted the results. W.-N.J., M.J., and F.-D.S. wrote the paper. G.M., H.-G.L., L.V.K and Z.K. edited the manuscript.

Declaration of interests

The authors declare no competing interests.

Figures

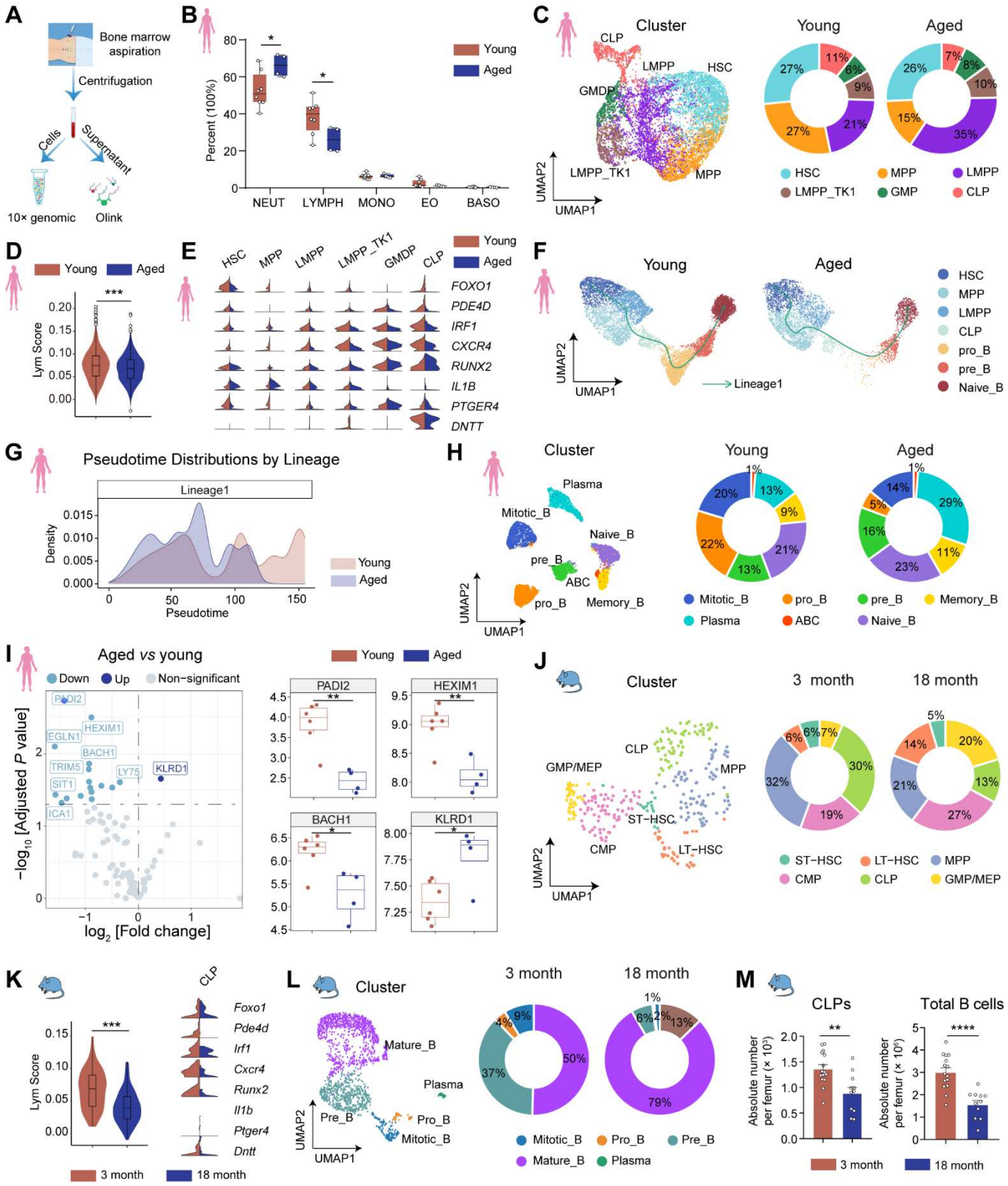


Figure 1 | Defective B cell lymphopoiesis is a hallmark of aged bone marrow in humans and mice. (A) Experimental scheme for single-cell RNA sequencing and Olink proteomics analysis of bone marrow cells from healthy young and aged individuals (< 40 years, n=8 and > 60 years, n=4). (B) Percentages of neutrophils (NEUT), lymphocytes (LYMPH), monocytes (MONO), eosinophils (EO), and basophils (BASO) in peripheral blood from healthy individuals. (C) Left: UMAP visualization of human bone marrow cell populations annotated by single-cell transcriptomics. Right: Six clusters with cell-type annotations are shown. Percentage of HSCs,

MPPs, LMPPs, LMPP_TK1s, GMPs and CLPs in bone marrow from young (left) and aged (right) individuals. HSC, hematopoietic stem cell; MPP, multipotential progenitor; LMPP, lymphoid-primed multipotential progenitor; LMPP_TK1, lymphoid-primed multipotent progenitor; GMP, granulocyte-macrophage dendritic cell progenitor; CLP, common lymphoid progenitor. (D) Violin plots showing lymphoid lineage gene signature scores (Lyn score) in bone marrow cells from young and aged individuals. (E) Violin plots showing expression levels of representative genes regulating hematopoietic differentiation in human bone marrow. (F) Predicted differentiation lineage during pseudotime analysis in human bone marrow. (G) Pseudotime distributions by lineage in humans bone marrow. (H) Left: UMAP visualization of B-lineage cells in human bone marrow. Right: Compositional differences in B-lineage subpopulations between young and aged bone marrow. (I) Olink proteomics analysis of human bone marrow interstitial fluid showing significant changes in proteins associated with proliferation, differentiation, and inflammation in young versus aged individuals. (J) Left: UMAP visualization of developmental stages along the hematopoietic stem cell (HSC) differentiation continuum in mice. Right: Compositional changes across HSC differentiation stage between 3-month-old and 18-month-old mice. (K) Left: Lymphoid gene signature scores (Lyn score) in bone marrow cells from 3-month-old and 18-month-old mice . Right: Violin plots showing expression of representative differentially expressed genes in CLPs of mice bone marrow. (L) Left: UMAP visualization of B-lineage subpopulations in mice. Right: Expression of canonical marker genes defining each B-lineage developmental stage. (M) Proportional abundance of CLPs and total B cells in bone marrow from 3-month-old and 18-month-old mice. Data are represented as mean ± SD. *$P < 0.05$, **$P < 0.01$, ***$P < 0.0001$, ****$P < 0.0001$ by two-way ANOVA (B) or by unpaired Student’s t test (D, E, I, K, and M).

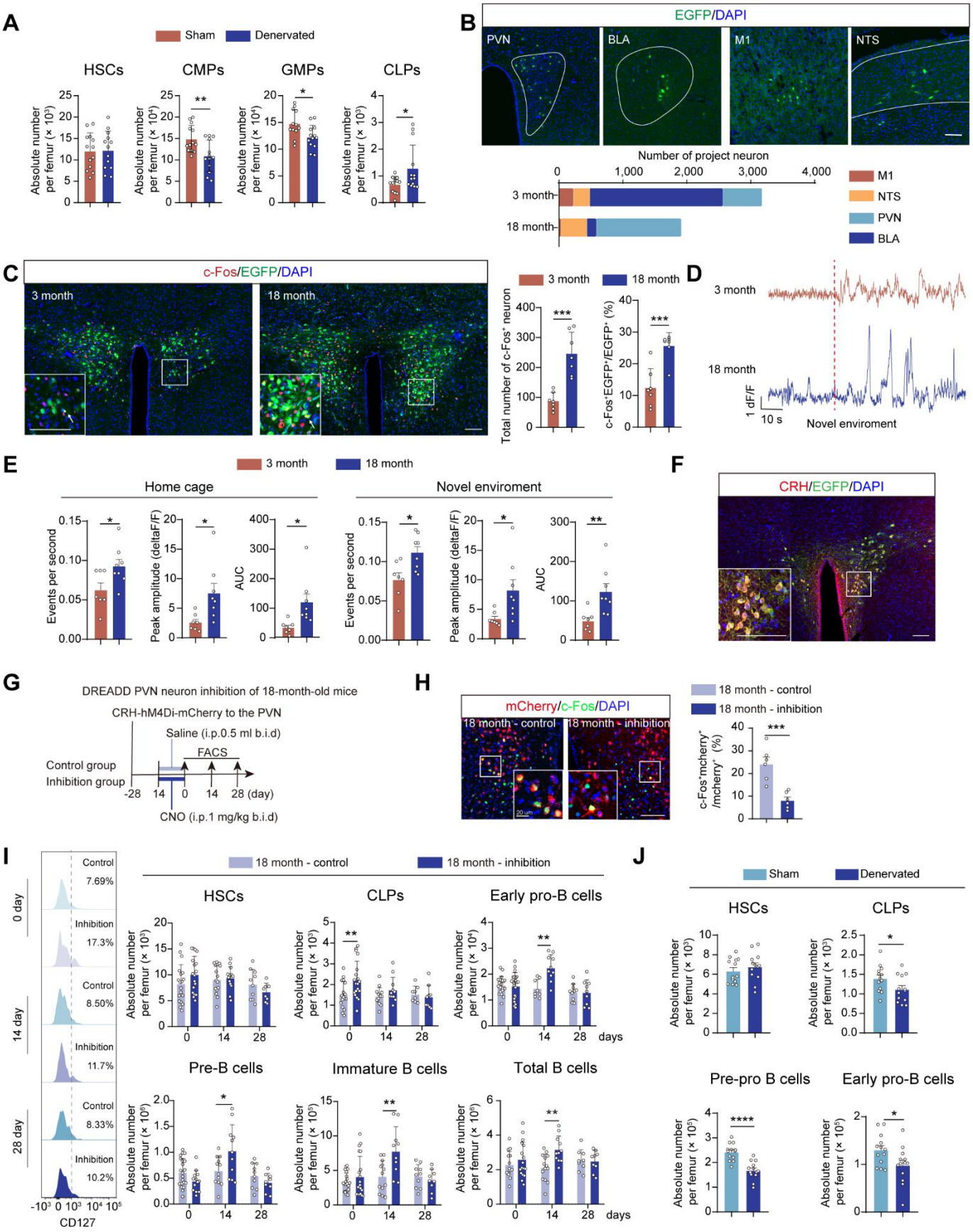


Figure 2 | Chemogenetic manipulation of PVN-CRH neuronal activity modulates B cell lymphopoiesis in bone marrow of 18-month-old mice. (A) Bar graphs showing numbers of bone marrow stem and progenitor cells in denervated versus sham-operated 18-month-old mice assessed by flow cytometry (n= 12 per group). (B) Above: Pseudorabies virus (PRV) retrograde tracing from mouse bone marrow showing EGFP-labeled neurons projecting to central nervous

system nuclei. Below: Quantification of PRV-EGFP labeled neurons is shown for the NTS, nucleus tractus solitarius; PVN, paraventricular nucleus of hypothalamus; BLA, basal lateral amygdala; M1, motor cortex 1. Scale bar, 100 μm. (C) Left: Immunofluorescence staining of PRV retrogradely labeled neurons (green) and c-Fos (red) in the PVN. DAPI (blue) marks cell nucleus. Scale bar, 200 μm. Right: Quantification of total c-Fos$^+$ neurons in the PVN of PRV-traced mice and the percentage of c-Fos$^+$ EGFP$^+$ neurons among EGFP$^+$ neurons (n= 7 per group). (D) Representative diagram of calcium signaling of the PVN neurons in 3-month-old and 18-month-old mice. (E) Quantification of calcium signaling activity in PVN neurons. (F) Immunofluorescence image showing co-localization of CRH (red) and PRV-EGFP labeled neurons (green) in the PVN. Scale bar, 200 μm. (G) Schematic diagram illustrating chemogenetic inhibition of PVN-CRH neurons in 18-month-old mice and the experimental timeline for flow cytometric analysis. (H) Effects of inhibitory manipulation. Left: Immunofluorescence images showing c-Fos$^+$ mCherry$^+$ neurons in the PVN. Right: Quantification of c-Fos$^+$ mCherry$^+$ neurons in 18-month-old mice following chemogenetic inhibition compared with control (n= 6 per group). (I) Flow cytometric analysis of bone marrow cell populations following chemogenetic inhibition in 18-month-old mice. Bar graphs showing numbers of bone marrow cell lineages (HSCs, CLPs, early pro-B cells, pre-B cells, immature B cells, total B cells) at days 0, 14, and 28 after chemogenetic inhibition of PVN-CRH neurons (n= 9 per group). (J) Flow cytometric quantification of bone marrow populations (HSCs, CLPs, pre-pro-B cells, early pro-B cells) in denervated versus sham-operated mice after chemogenetic inhibition of PVN-CRH neurons in 18-month-old mice. Data are represented as mean ± SD. *P < 0.05, **P < 0.01, ***P < 0.0001, ****P < 0.0001 by unpaired Student’s t test (A, C, E, H and J), or by two-way ANOVA (I).

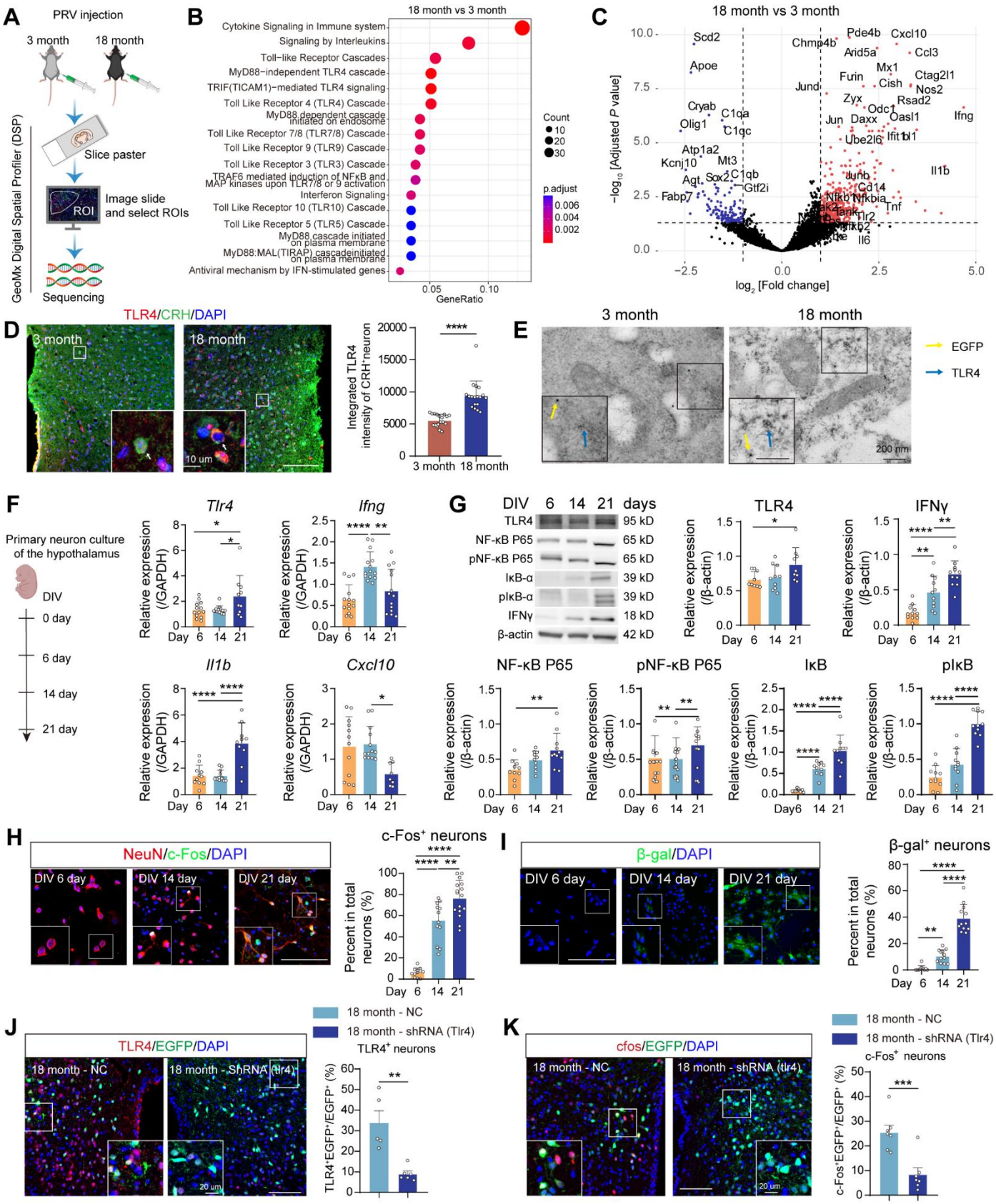


Figure 3 | Aging activates PVN-CRH neurons through TLR4/IFNγ signaling. (A) Workflow illustrates identification of PRV-EGFP labeled neurons in the PVN using spatial transcriptomic analysis. (B) KEGG pathway enrichment analysis of differentially expressed genes. (C) Volcano plot showing differentially expressed genes of PRV-EGFP labeled neurons in the PVN of 3-month-old or 18-month-old mice. (D) Left: Immunofluorescence image showing TLR4 (red) expression in CRH$^+$ neurons (green). Scale bar, 100 μm. Right: Quantification of integrated TLR4 fluorescence

intensity in CRH$^+$ neurons from 3-month-old or 18-month-old mice (n= 18 per group). (E) Representative immunoelectron microscopy images illustrating ultrastructural features of PVN neurons in 3-month-old or 18-month-old mice. Yellow arrows indicate EGFP$^+$ particles; blue arrows indicate TLR4$^+$ particles. Scale bar, 200 nm. (F) Left: Schematic timeline for culturing and stimulation of dissociated primary hypothalamic neurons. Right: qPCR analysis of *Tlr4*, *Ifng*, *Il1b*, and *Cxcl10* expression at indicated time points (n= 12 per group). (G) Left: Representative western blots of TLR4, IFNγ, total and phosphorylated NF-κB p65 (p-NF-κB), and total and phosphorylated IκB (p-IκB). Right: Densitometric quantification of protein levels (n= 6 per group). (H) Left: Representative immunofluorescence images of c-Fos$^+$ neurons at indicated time points. Right: Quantification of c-Fos$^+$ neurons (n=12 per group). Scale bar, 100 μm. (I) Left: β-galactosidase (β-gal) staining indicating senescent neurons at indicated time points. Right: Quantification of β-gal$^+$ cells (n= 12 per group). Scale bar, 100 μm. (J) Left: Immunofluorescence staining of CRH-shRNA (Tlr4)-EGFP (green) and TLR4 (red) in the PVN of 18-month-old mice. Scale bar, 100 μm. Right: Quantification of TLR4$^+$ EGFP$^+$ neurons in EGFP$^+$ neurons in NC and shRNA (Tlr4) group. (K) Left: Immunofluorescence staining of CRH-shRNA (Tlr4)-EGFP viruses (green) and c-Fos (red) in the PVN of 18-month-old mice. Scale bar, 100 μm. Right: Quantification of c-Fos$^+$ EGFP$^+$ neurons in EGFP$^+$ neurons in NC and shRNA (Tlr4) group. Data are represented as mean ± SD. **P < 0.01, ***P < 0.001, ****P < 0.0001 by unpaired Student's t test (D, J, K). *P < 0.05, **P < 0.01, ***P < 0.001, ****P < 0.0001 by one-way ANOVA (F-I).

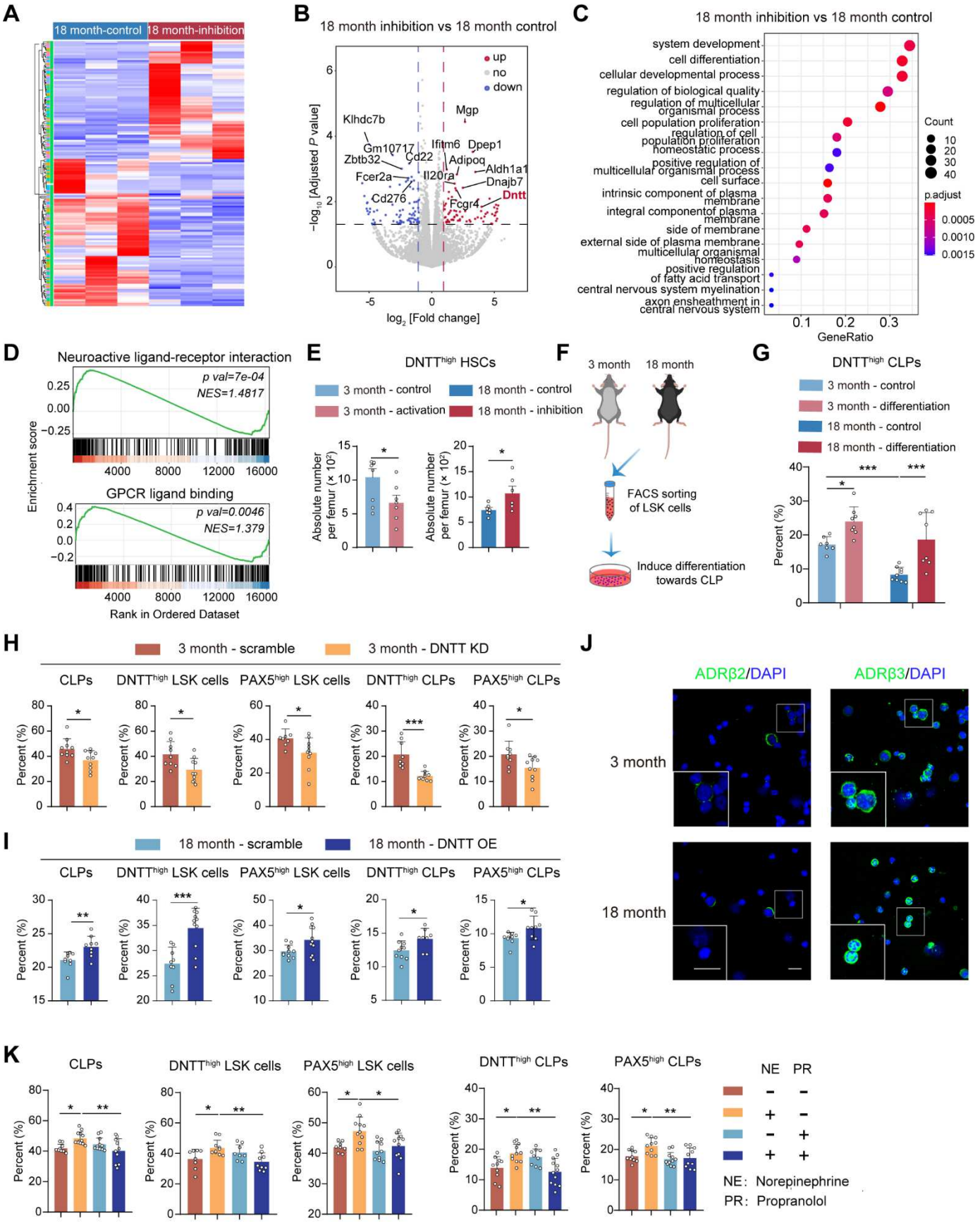


Figure 4 | PVN-CRH neurons regulate B cell lymphopoiesis of bone marrow HSPCs through DNA nucleotidylexotransferase (DNTT). (A, B) Transcriptomic analysis of sorted HSCs showing differential gene expression between control and PVN-CRH inhibition groups. Upregulated genes (red) are displayed as a heatmap (A) and volcano plot (B). (C, D) Gene Ontology (GO) enrichment analysis (C) and Gene Set Enrichment Analysis (GSEA) (D) of differentially expressed genes. (E)

Flow cytometric quantification of DNTT^{high} HSCs in 3-month-old mice after PVN-CRH neuron activation (left) and in 18-month-old mice after PVN-CRH neuron inhibition (right), compared with their respective controls (n= 7 per group). (F) Schematic diagram illustrating differentiation of LSK cells (FACS sorted from bone marrow of 3-month-old and 18-month-old mice) into common lymphoid progenitors (CLPs). (G) Proportion of DNTT^{high} CLP cells in cultured LSK cells of 3-month-old and 18-month-old mice, analyzed under differentiation and control conditions. (H) Flow cytometry analysis following induction of differentiation after DNTT knockdown (KD) in cultured LSK cells of 3-month-old mice. Bar graphs show counts of CLPs, DNTT^{high} LSK cells, PAX5^{high} LSK cells, DNTT^{high} CLP cells, and PAX5^{high} CLP cells at 72 h after DNTT KD or scramble control in 3-month-old mice (n= 10 per group). (I) Flow cytometry analysis following induction of differentiation after DNTT overexpression in cultured LSK cells of 18-month-old mice. Bar graphs show counts of CLPs, DNTT^{high} LSK cells, PAX5^{high} LSK cells, DNTT^{high} CLP cells, and PAX5^{high} CLP cells at 72 h after DNTT overexpression (OE) or scrambled control in 18-month-old mice (n= 10 per group). (J) Representative immunofluorescence images of ADRβ2^{+} or ADRβ3^{+} LSK cells of 3-month-old or 18-month-old mice. Scale bar, 20 μm. (K) Bar graphs showing counts of CLPs, DNTT^{high} LSK cells, PAX5^{high} LSK cells, DNTT^{high} CLP cells, and PAX5^{high} CLP cells after treatment with propranolol, norepinephrine or DMSO in cultured LSK cells of 3-month-old mice (n= 9 per group). Data are represented as mean ± SD. *P < 0.05, **P < 0.01, ****P < 0.0001 by unpaired Student’s t test (E, H, and I), one-way ANOVA (K), or by two-way ANOVA (G).

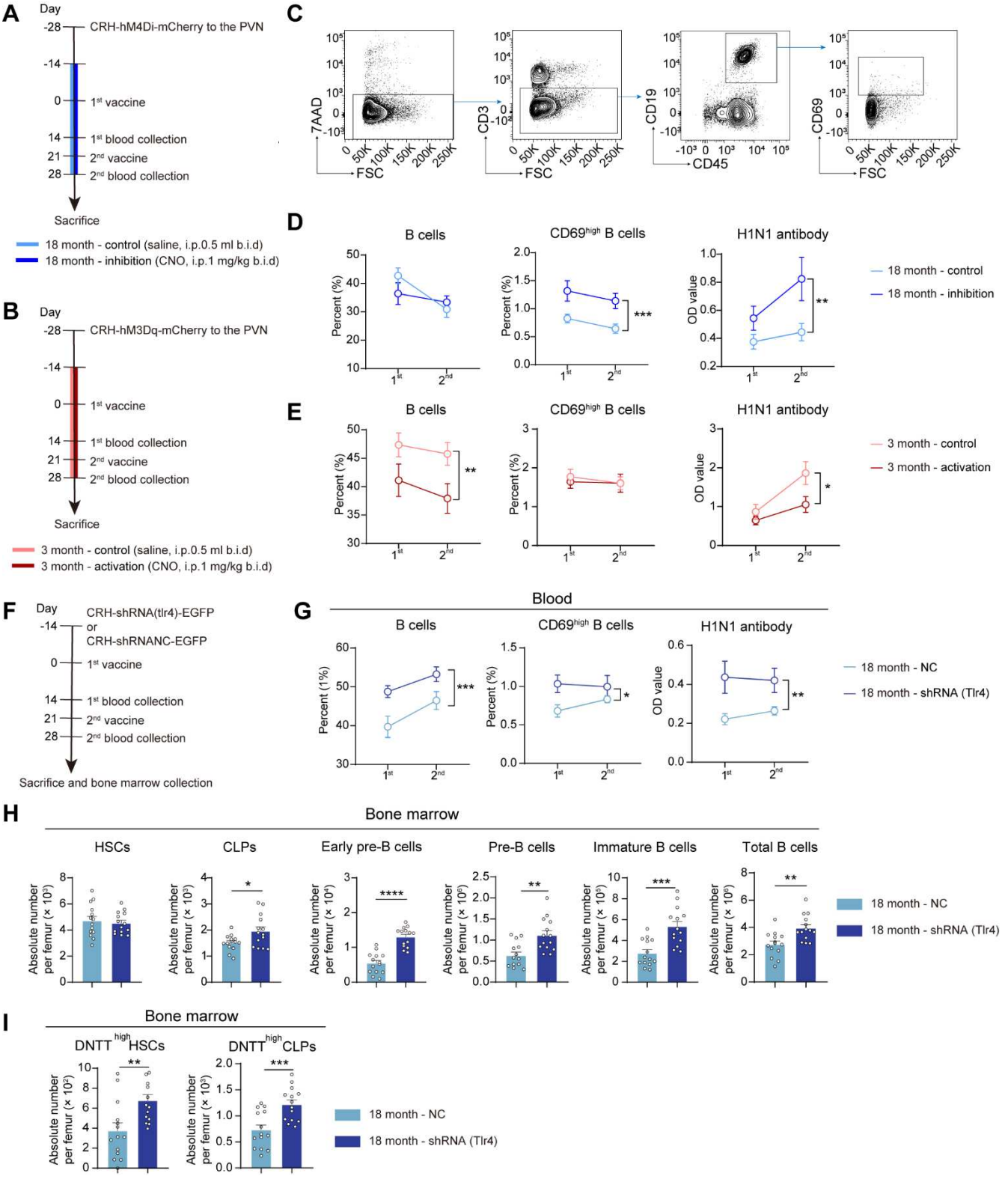
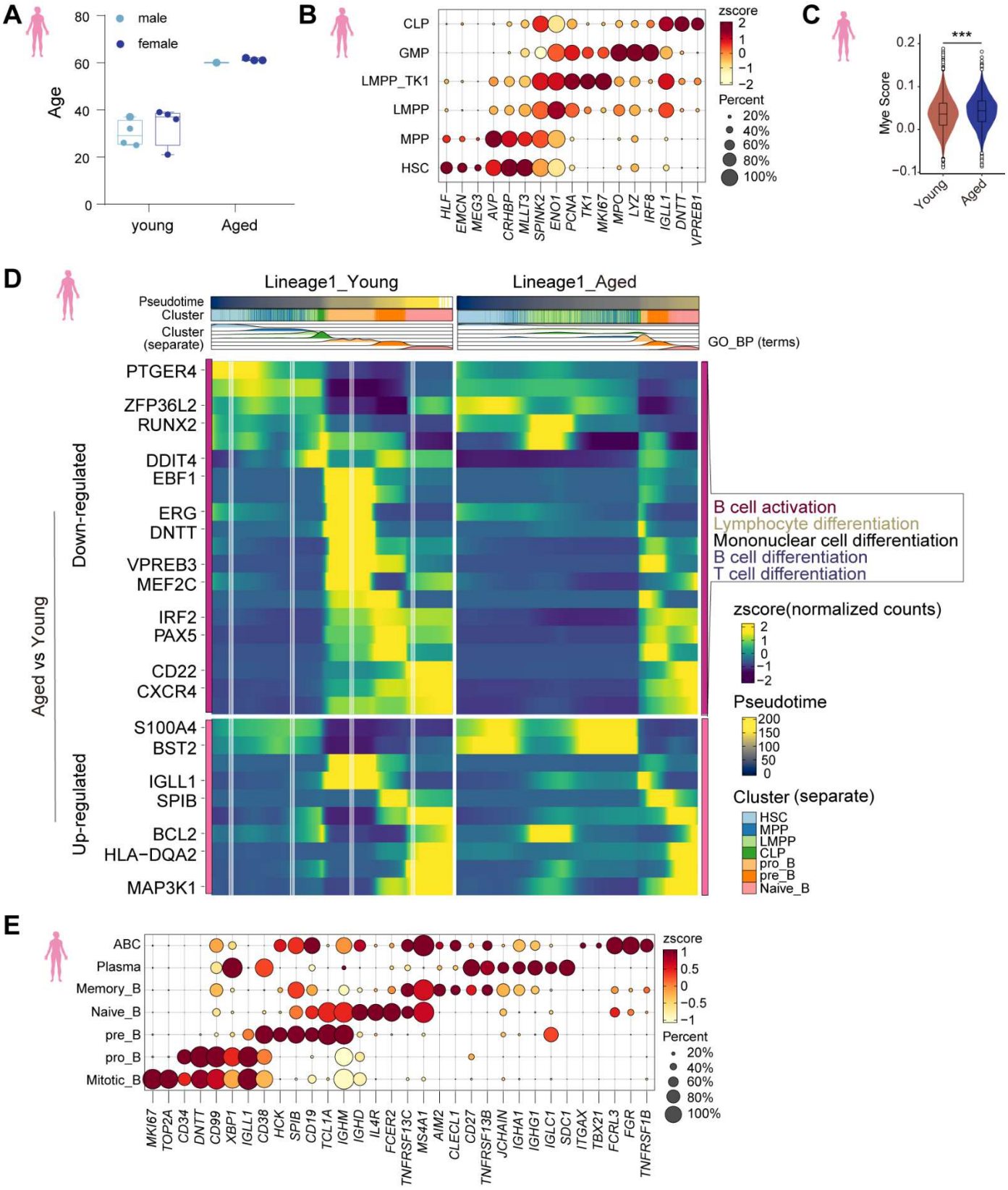


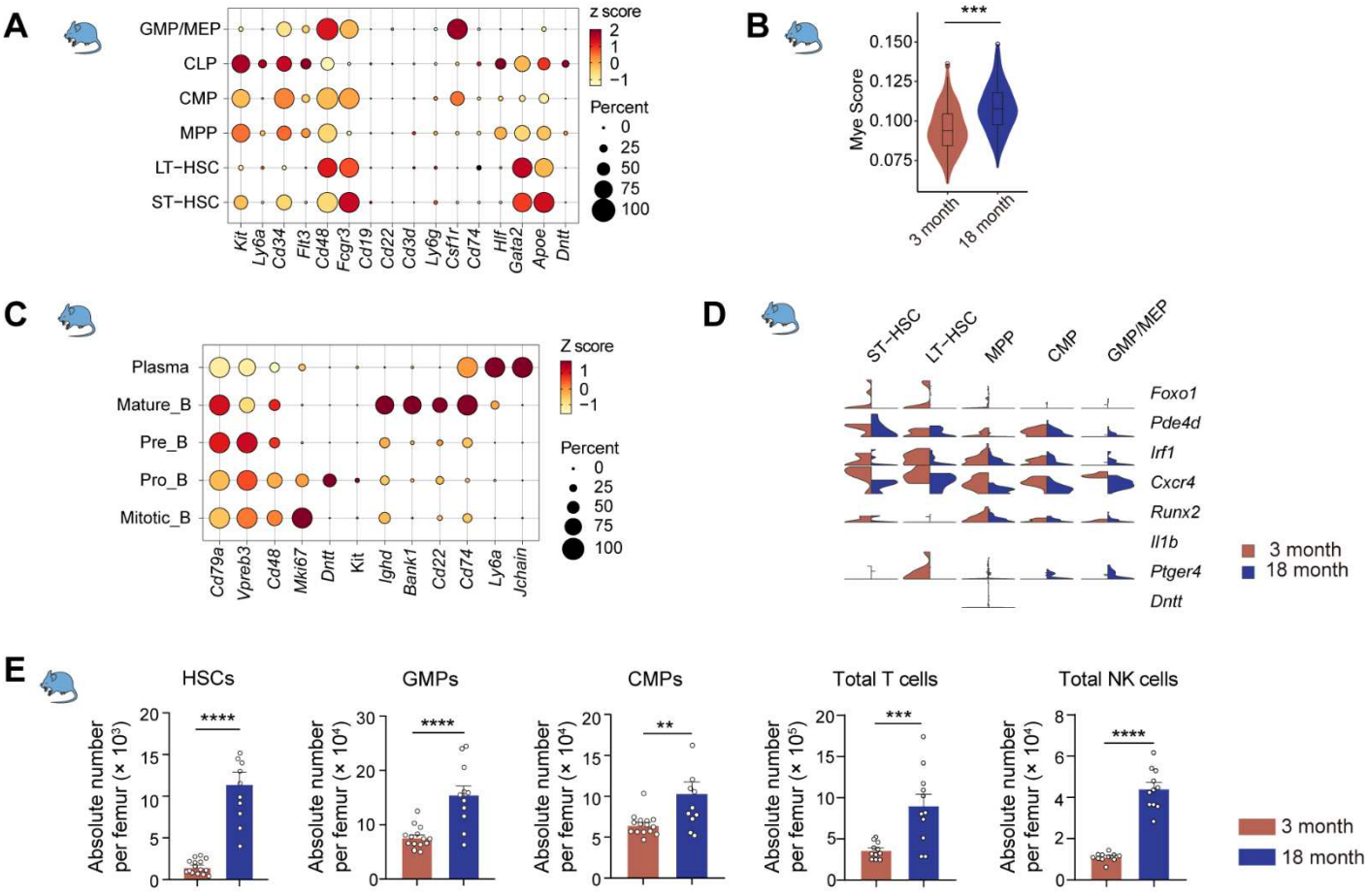
Figure 5 | Targeting PVN-CRH neuronal hyperactivity restores H1N1 vaccine response in 18-month-old mice. (A, B) Experimental timeline for vaccine challenge in 18-month-old (A) and 3-month-old (B) mice following chemogenetic manipulation (inhibition or activation, respectively) of PVN-CRH neuronal activity. (C) Gating strategy for flow cytometric analysis of total B cells and activated B cells ($CD69^{+}$) in peripheral blood. (D, E) Levels of total B cells, activated B cells, and H1N1-specific antibodies in peripheral blood measured during two rounds of vaccination in control versus PVN inhibition groups of 18-month-old mice (D) and control versus PVN activation groups of 3-month-old mice (E). (F) Schematic illustration of the vaccine challenge experiment following injection of CRH neuron–specific TLR4 knockdown (KD) AAV into the PVN of 18-month-old mice

(n = 14). (G) Levels of B cells, activated B cells, and H1N1-specific antibodies during vaccine challenge in peripheral blood of control versus CRH-TLR4 KD of 18-month-old mice. (H) Bar graphs showing numbers of bone marrow cell populations (HSCs, CMPs, CLPs, pre-B cells, immature B cells, total B cells) after TLR4 KD in 18-month-old mice. (I) Bar graphs showing numbers of $DNTT^{high}$ HSCs and $DNTT^{high}$ CLPs in bone marrow after TLR4 KD in 18-month-old mice. Data are represented as mean ± SD. *P < 0.05, **P < 0.01, ***P < 0.01 by two-way ANOVA (D, E, and G) or by unpaired Student's t test (H and I).

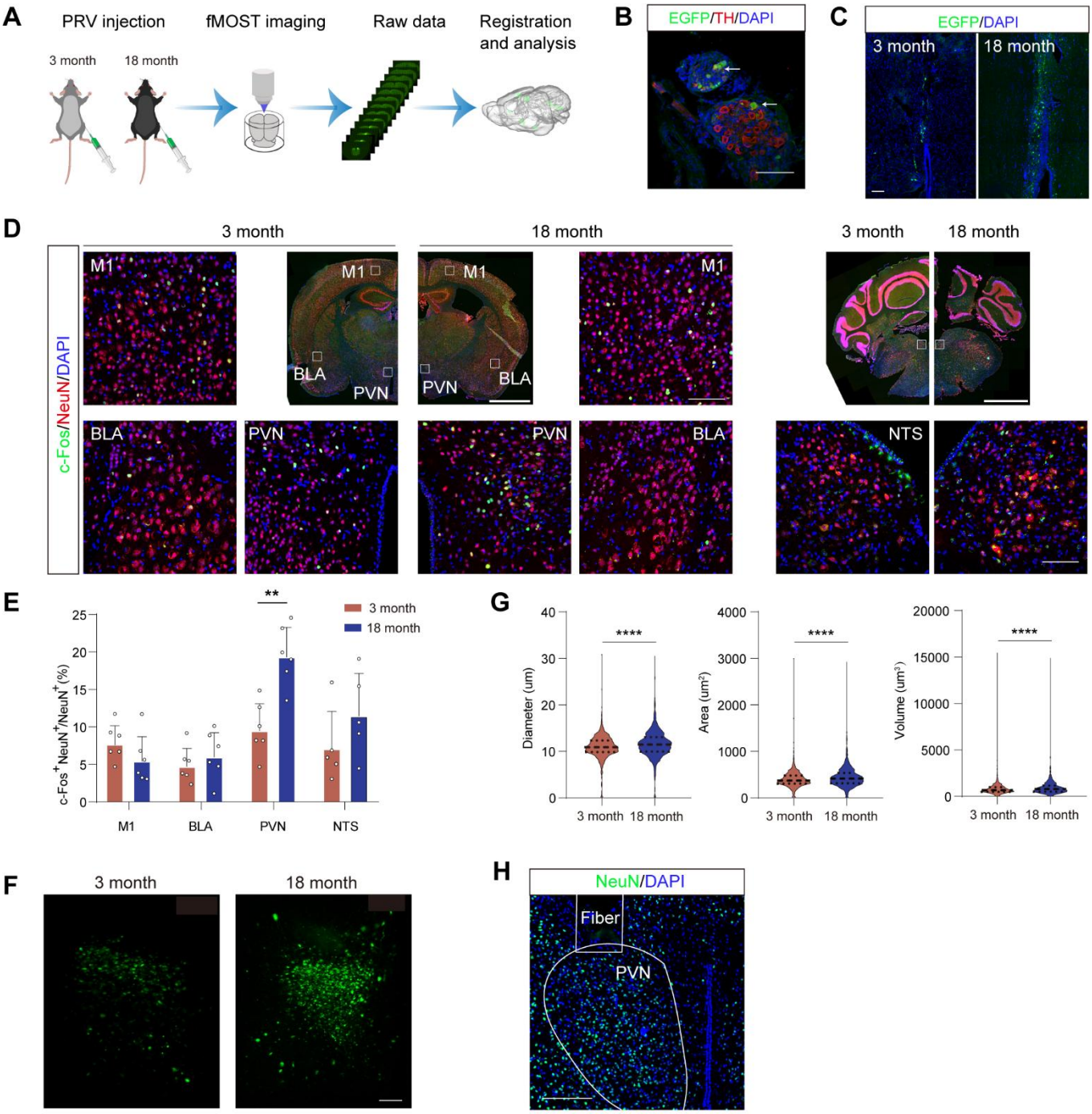


Supplementary Figure 1 | Characterization of bone marrow HSPCs and B cell lymphopoiesis in young and aged individuals. (A) Age and sex distribution of healthy volunteers. (B) Dot plot showing expression of canonical marker genes for hematopoietic stem and progenitor cells (HSPCs) in human samples. (C) Myeloid gene signature scores (Mye score) in bone marrow cells from young and aged individuals. (D) Expression of genes co-related with lineage differentiation during pseudotime analysis of human bone marrow. (E) Dot plot showing

expression of canonical marker genes for distinct B-cell subsets in human samples. Data are presented as mean ± SD. ***P < 0.001 by unpaired Student's t test (C).

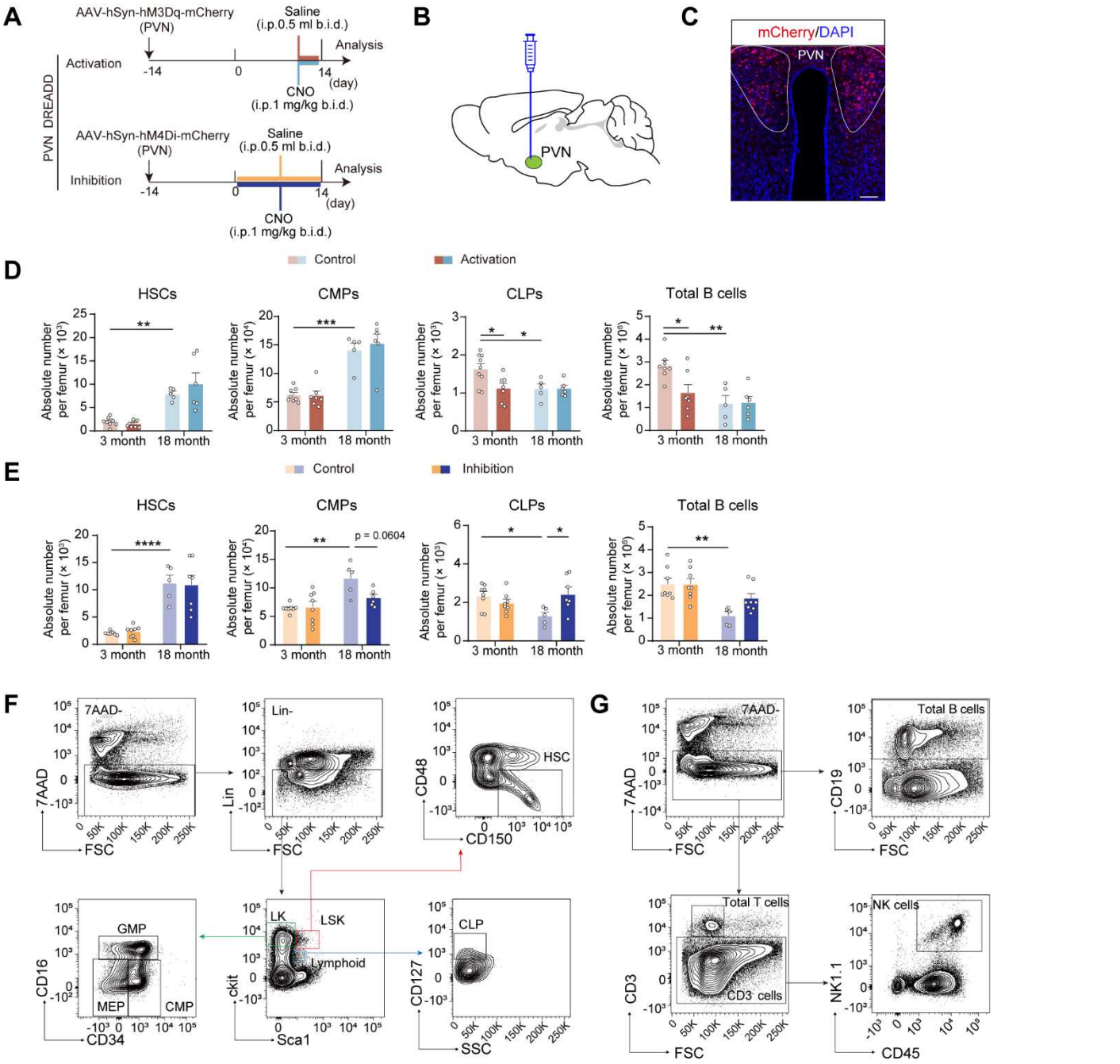


Supplementary Figure 2 | Characterization of bone marrow cells in 3-month-old and 18-month-old mice. (A) Dot plot showing expression of canonical marker genes for HSPCs in mice. (B) Myeloid gene signature scores (Mye score) in bone marrow from 3-month-old and 18-month-old mice. (C) Dot plot showing expression of canonical marker genes for distinct B-cell subsets in mice. (D) Violin plots showing expression of representative differentially expressed genes across hematopoietic differentiation stages in mice. (E) Proportional abundance of HSCs, GMPs, CMPs, total T cells and total NK cells in bone marrow from 3-month-old and 18-month-old mice. Data are presented as mean ± SD. **P < 0.01, ***P < 0.001, ****P < 0.0001 by unpaired Student's t test (B, D and E).

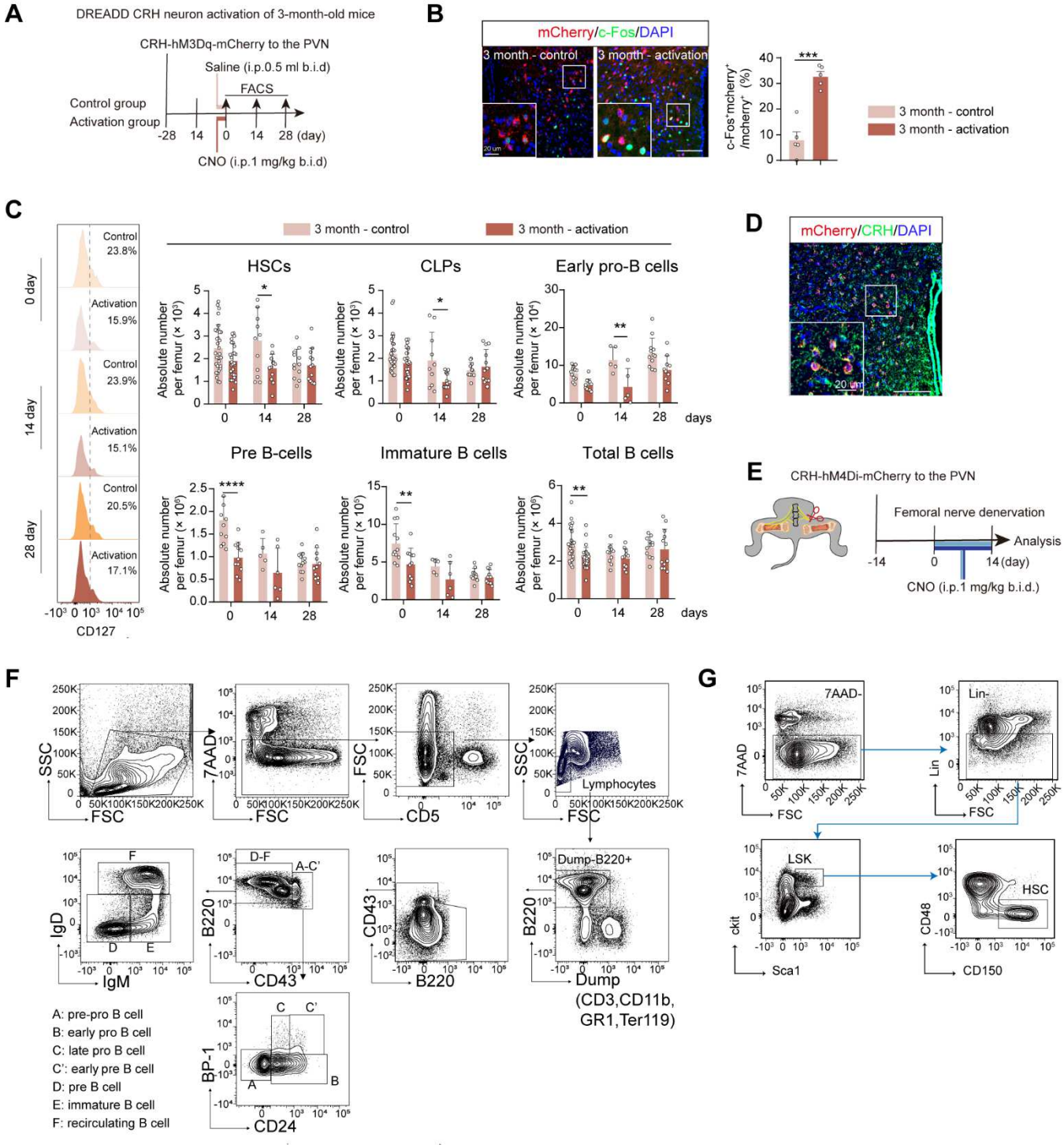


Supplementary Figure 3 | Whole-brain mapping and characterization of PRV labeled neurons. (A) Workflow of fluorescence micro-optical sectioning tomography (fMOST) for whole-brain imaging and 3D reconstruction of PRV-EGFP labeled neurons. (B) Immunofluorescence staining of sympathetic ganglia showing PRV-EGFP labeled neurons co-stained with the sympathetic marker tyrosine hydroxylase (TH, red). Scale bar, 100 μm. (C) Location and morphology of PRV-EGFP labeled neurons in the spinal cord. Scale bar, 100 μm. (D) Immunofluorescence images showing c-Fos$^+$ (green) neurons in the M1, BLA, PVN and NTS of 3-month-old and 18-month-old mice. Scale bar, 2 mm or 100 μm. (E) Quantitative analysis of c-Fos$^+$NeuN$^+$/NeuN$^+$ percentage in the M1, BLA, PVN and NTS. (F) Representative 3D reconstructions showing the distribution of PRV-EGFP labeled neurons in the brains of 3-month-old and 18-month-old mice. Scale bar, 100 μm. (G) Quantitative morphometric analysis of reconstructed PRV-EGFP labeled neurons (green), including diameter, surface area, and volume.

(H) Location of GCam recording fiber in the PVN (NeuN, green). Scale bar, 100 μm. Data are presented as mean ± SD. **P < 0.01 by two-way ANOVA (E). ****P < 0.0001 by unpaired Student's t test (G).

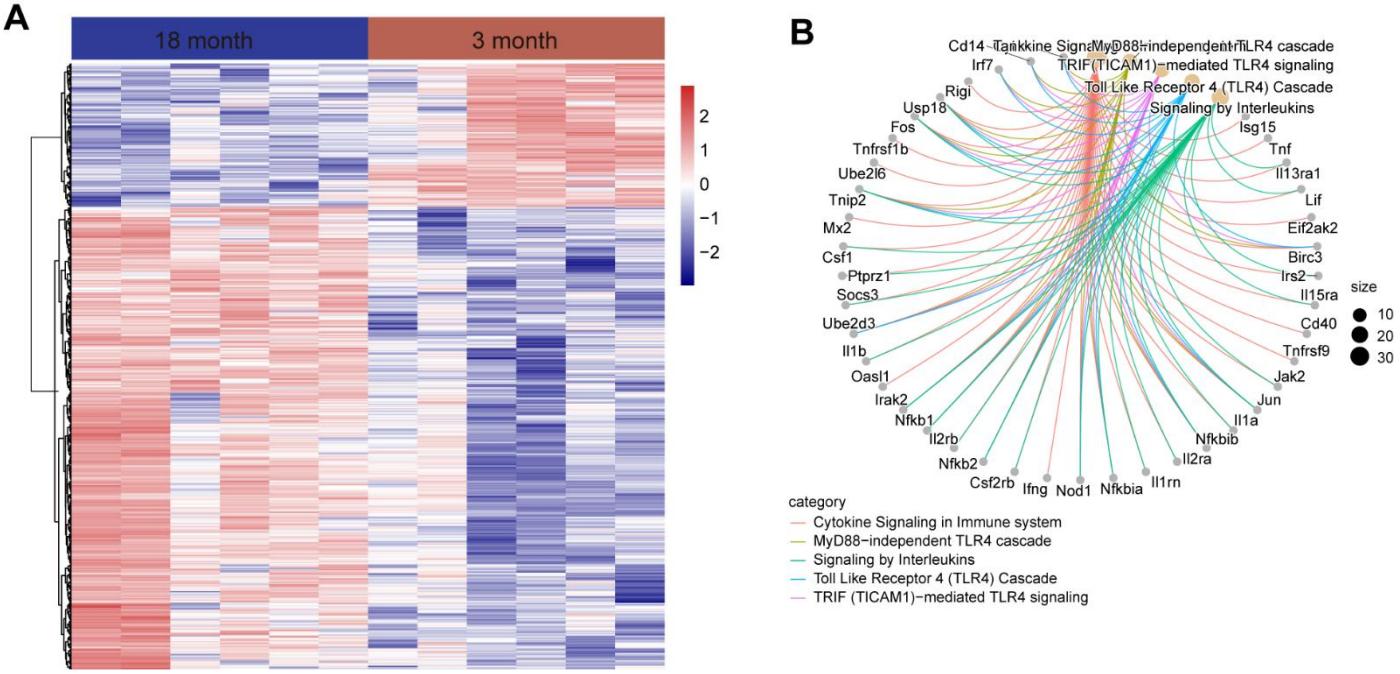


Supplementary Figure 4 | Manipulating activity of the PVN neurons modulated B cell lymphopoiesis in mice. (A) Schematic illustrating chemogenetic manipulation of PVN neuronal activity. (B) Schematic indicating the injection site within the PVN of the mouse brain. (C) Immunofluorescence images showing AAV-hSyn chemogenetic virus transfection in the PVN. (D) Bar graphs showing numbers of bone marrow cell populations (HSCs, CMPs, CLPs, total B cells) 5 days after chemogenetic activation of PVN neurons. (E) Bar graphs showing numbers of bone marrow cell populations (HSCs, CMPs, CLPs, total B cells) 14 days after chemogenetic inhibition of PVN neurons. (F) Gating strategy used to identify hematopoietic populations derived from hematopoietic progenitor cells (HSPCs). (G) Gating strategy for identification of total B cells, T cells, and NK cells. Data are represented as mean ± SD. *P < 0.05, **P < 0.01, ****P < 0.0001 by two-way ANOVA (D and E).

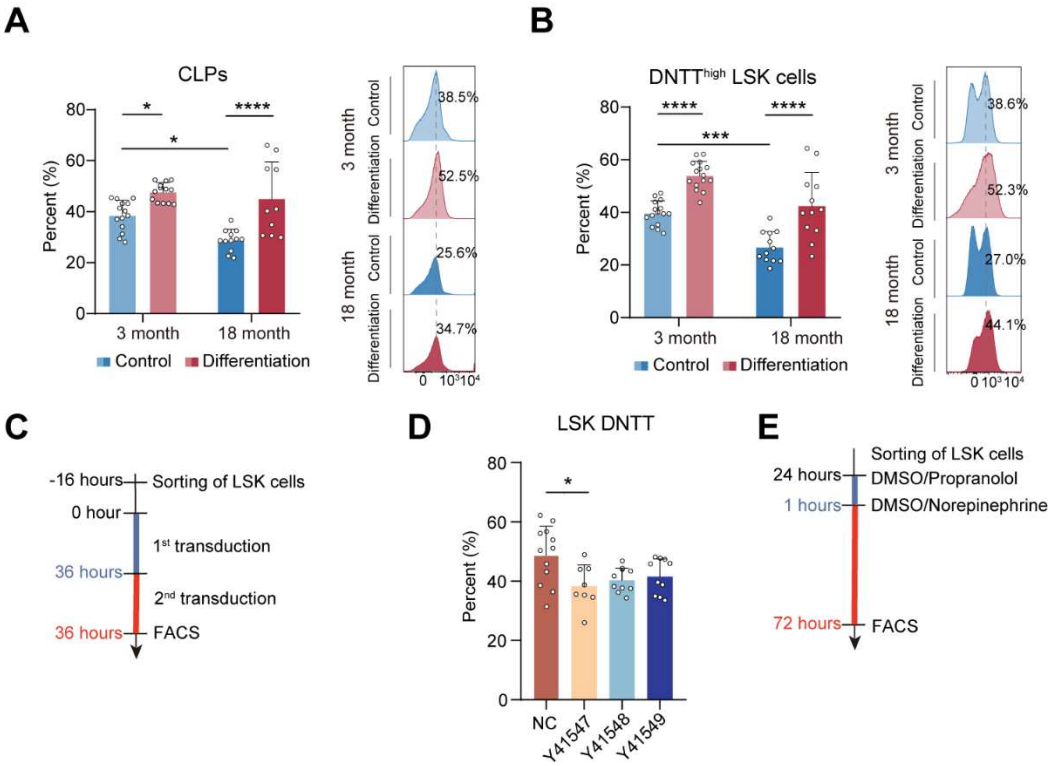


Supplementary Figure 5 | PVN-CRH neurons hyperactivation in 3-month-old mice suppresses B cell lymphopoiesis. (A, B) Effects of excitatory manipulation. (A) Schematic diagram illustrating chemogenetic activation of PVN-CRH neurons in 3-month-old mice and the experimental timeline for flow cytometric analysis. (B) Left: Immunofluorescence images showing c-Fos$^+$ mCherry$^+$ neurons in the PVN. Right: Quantification of c-Fos$^+$ mCherry$^+$ neurons following chemogenetic activation compared with control (n= 5 per group). (C) Flow cytometry analysis of bone marrow cell populations following chemogenetic activation in the PVN of 3-month-old mice. Bar graphs showing numbers of bone marrow cell lineages (HSCs, CLPs, early pro-B cells, pre-B cells, immature B cells, total B cells) at days 0, 14, and 28 after chemogenetic activation of PVN-CRH neurons in 3-month-old mice (n= 10 per group). (D) Immunofluorescence image showing co-localization of CRH-hM4Di/hM3Dq-mCherry viruses (red) with CRH neurons (green) in the PVN.

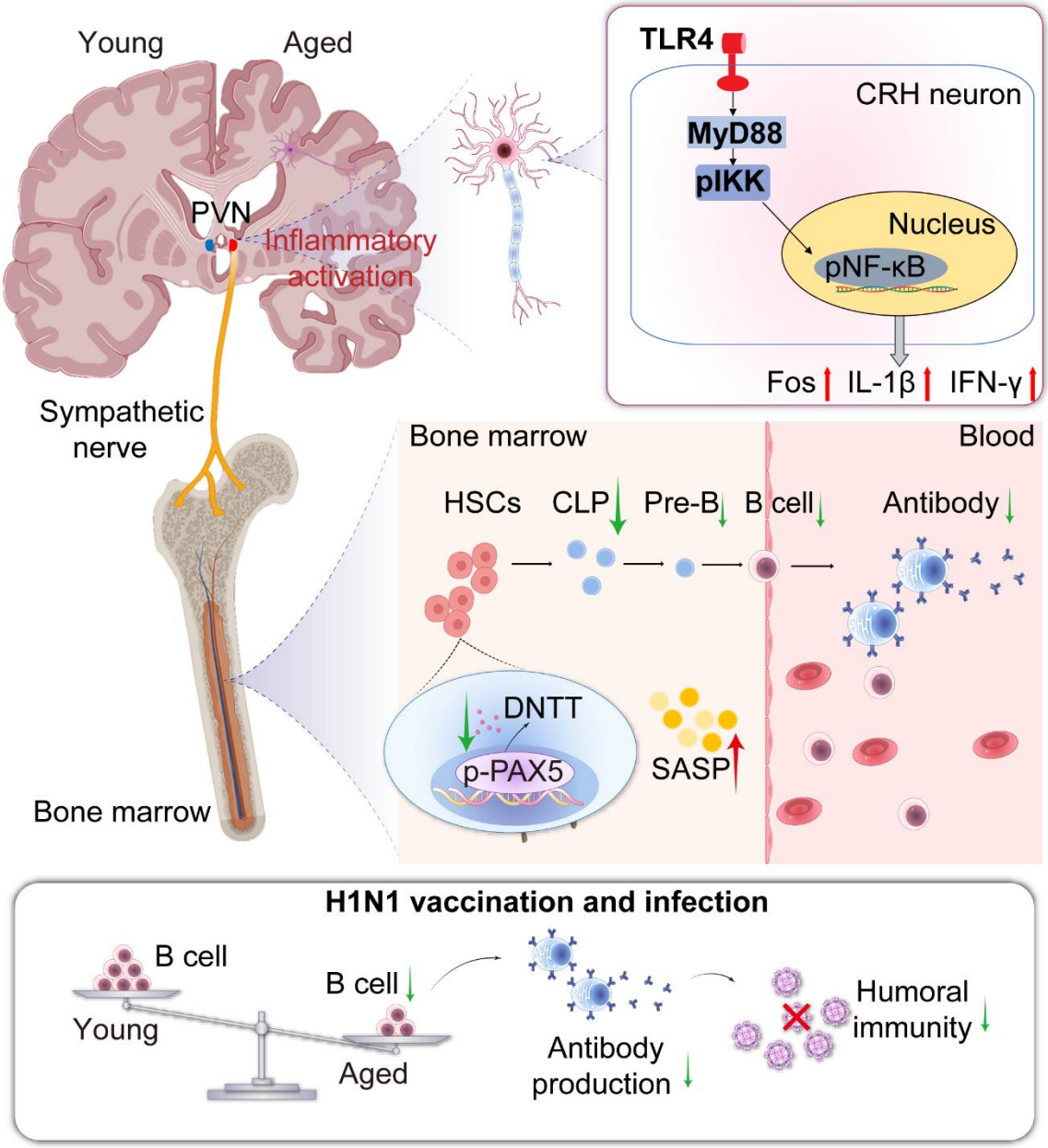
Scale bar, 100 μm. (E) Schematic of the bone marrow denervation procedure following chemogenetic inhibition of PVN neurons in 18-month-old mice. CNO, clozapine-N-oxide. (F) Schematic of the flow cytometry gating strategy used to define distinct B-lineage developmental stages, from pre-pro B cells to recirculating B cells in the bone marrow. (G) Gating strategy for isolation of HSCs ($Lin^{-}ckit^{+}Sca1^{+}CD48^{-}CD150^{+}$).*P < 0.05, **P < 0.01, ***P < 0.001, ****P < 0.0001 by unpaired Student's t test (B) or by two-way ANOVA (C).



Supplementary Figure 6 | Transcriptomic profiling of PRV-EGFP labeled neurons in the PVN reveals a pro-inflammatory signature during aging. (A) Heatmap showing differentially expressed genes in PRV-EGFP labeled PVN neurons from 3-month-old and 18-month-old mice. (B) Network showing associations between differentially expressed genes and significantly enriched inflammatory signaling pathways.



Supplementary Figure 7 | DNTT participates in LSK differentiation. (A) Quantification of CLP proportions in 3-month-old and 18-month-old mice under differentiation and control conditions. (B) Quantification of DNTT^{high} LSK cells proportions in 3-month-old and 18-month-old mice under differentiation versus control conditions. (C) Schematic illustrating transfection of sorted LSK cells. (D) Validation of DNTT knockdown efficiency following lentiviral transfection. Sequence verification confirms the specificity and efficiency of the lentiviral vector targeting DNTT**.** (E) Schematic illustrating pharmacological inhibition or activation of β-adrenergic receptors in cultured LSK cells of 3-month-old mice. Data are represented as mean ± SD. **P* < 0.05, ***P* < 0.01, ****P* < 0.001, *****P* < 0.0001 by one-way ANOVA (D) or by two-way ANOVA (A and B).



Supplementary Figure 8 | Aging activates a hypothalamus-bone marrow neuroimmune circuit that impairs B cell lymphopoiesis. (A) Defective B cell lymphopoiesis is a hallmark of aged bone marrow in both humans and mice. (B) The paraventricular nucleus (PVN) - bone marrow axis becomes hyperactivated during aging. (C) Aging activates TLR4 signaling and induces inflammatory activation of the PVN neurons. (D) DNA nucleotidylexotransferase (DNTT) in hematopoietic stem and progenitor cells (HSPCs) mediates neural activity-regulated B cell lymphopoiesis. (E) Reducing neural hyperactivity improves vaccine-induced immune responses in aged mice.

Experimental Model and Subject Details

Human bone marrow and peripheral blood samples

The study was conducted in accordance with the Declaration of Helsinki of the World Medical Association. The inclusion of human subjects and all supporting documentation were approved by the Ethics Committee of Beijing Tiantan Hospital (KY2021-166). Written informed consent was obtained from all participants prior to enrollment. Bone marrow samples for single-cell RNA sequencing were collected from 4 older individuals and 8 younger individuals (7 female and 5 male) [15,21,43]. Inclusion criteria were: 1) age ≥ 18 years; 2) generally healthy status with a body mass index (BMI) of 18-34 and normal routine laboratory test results.

Mice

C57BL/6 mice (3-month or 18-months old) were purchased from the Experimental Animal Laboratories of Sibeifu (Beijing, China) Biotechnology Co., Ltd. Mice were maintained under specific pathogen–free conditions at 20-26°C with a 12-hour light/dark cycle. All experimental procedures were conducted in accordance with the guidelines of the Institutional Animal Care and Use Committee of Beijing Tiantan Hospital and the Chinese Small Animal Protection Association. The study protocol was approved by the Ethical committee of IRCBC (Beijing Tiantan Hospital; approval number: 202203004).

Single cell RNA sequencing of human bone marrow

Single-cell nuclei were isolated from fresh human bone marrow suspensions using the Chromium Nuclear Isolation Kit (10× Genomics, #PN-1000494) for single-nucleus RNA sequencing. Libraries were constructed by Berry Genomics Co., Ltd. Raw sequencing data were filtered and quality-controlled to obtain high-quality datasets. Cell types were annotated based on canonical marker genes for hematopoietic stem cells (HSCs), progenitor cells, and terminally differentiated cells, followed by clustering and identity assignment. To compare lymphoid transcriptomic profiles between young and aged bone marrow, a lymphoid gene set was obtained from Harmonizome 3.0. Differential gene expression (DEG) analysis and module scoring were performed using Seurat (AddModuleScore), and results were visualized using violin plots.

To reconstruct the continuous differentiation process of human bone marrow B-lineage cells, we performed trajectory inference analysis using the Slingshot R package (v2.12.0). Based on the UMAP embedding and prior knowledge identifying the HSPC cluster as the trajectory root, Slingshot constructed a lineage tree by fitting a principal curve through the data. Each cell was then assigned a pseudotime value, representing its relative progression along the inferred differentiation path and were visualized (doi:10.1186/s12864-018-4772-0 (2018).).

Single cell RNA sequencing of mice bone marrow

We analyzed the publicly available single-cell RNA sequencing data of the mice bone marrow generated by Chunying Yang et al., 2022[43]. The processed gene expression matrix and the corresponding cell-type metadata were downloaded from the Gene Expression Omnibus (GEO) under the accession number GSE169608. We clustered the subset while retaining the original

annotation labels for comparison and analyzed them using the same pipeline as human bone marrow.

Protein profiling of human bone marrow interstitial fluid

Protein expression in human bone marrow interstitial fluid was quantified using the Olink® Target 96 Mouse Exploratory Panel (Olink, Uppsala, Sweden), a high-throughput immunoassay based on proximity extension technology. This panel simultaneously measures 92 protein biomarkers using DNA-labeled antibody probes. Following the manufacturer's protocol, samples were incubated with oligonucleotide-conjugated antibody pairs. Upon target binding, proximity-dependent DNA hybridization generated amplifiable reporter sequences, which were quantified by real-time PCR. Amplification products were separated and detected using a 96.96 Dynamic Array IFC (Fluidigm, CA, USA) on a Biomark HD instrument. Raw data were preprocessed using Olink GenEx software. Proteins with a detection rate below 95% were excluded. Normalized Protein Expression (NPX) values were calculated from Ct values and reported on a $\log_2$ scale.

Pseudorabies Virus (PRV) tracing of mouse neurons and fluorescence micro-optical sectioning tomography (fMOST)

Pseudorabies virus (PRV), an attenuated live vaccine strain, was used as a retrograde neuronal tracer. C57BL/6 mice (3-month and 18-month-old) were anesthetized with 2,2,2-tribromoethanol. The right femoral bone marrow cavity was exposed, and a total of 3 μl PRV-CAG-EGFP (BrainVTA, P03001) viral solution was injected into three sites within the cavity to facilitate viral spread. Each injection site was sealed with dental cement to prevent leakage into surrounding tissues. The surgical incision was then closed using standard sutures. Tissue samples were collected five days after the virus injection. After perfusion, PRV-traced mouse samples were fixed in paraformaldehyde and dehydrated through a graded ethanol series. Samples were stained with Sudan Black B (SBB) and infiltrated with resin through graded concentrations at equal time intervals, followed by embedding in appropriate capsules. The temperature gradually increased to allow complete resin polymerization. After removal of the capsule molds, samples were trimmed and prepared for imaging. Whole-brain imaging was performed using a Bio Mapping 5000 fluorescence micro-optical tomography system. Samples were mounted on the sectioning stage and serially sectioned at 2 μm thickness. Images were acquired at a resolution of 0.35 × 0.35 × 2 μm. Acquired data were automatically reconstructed into image stacks. Preprocessing included brightness normalization, defect removal, background correction, noise reduction, contrast enhancement, and rotational alignment. Three-dimensional reconstruction was performed using Imaris File Converter. Regions of interest—including the cortex, paraventricular hypothalamic nucleus, basolateral amygdala, and nucleus tractus solitarius—were segmented using the Crop function in Imaris for subsequent spot detection and quantitative analysis of neuronal number and diameter.

Immunofluorescence staining

Brain, spinal cord, and sympathetic ganglia tissues were sectioned at 20 μm thickness using a freezing microtome (Leica, CM1860). Sections were washed three times with PBS for 10 min and

then permeabilized with 0.3% Triton X-100 in PBS for 30 min. After blocking with 5% donkey serum in PBS for 1 h, samples were incubated overnight at 4°C with primary antibodies (rabbit anti-mouse c-Fos Ab, Abcam, ab222699; rabbit anti-mouse CRH Ab, Sigma-Aldrich, C5348; rabbit anti-mouse TLR4 Ab, Abcam, ab22048). Sympathetic ganglia sections were incubated with primary antibodies (rabbit anti-mouse Tyrosine Hydroxylase Ab, Abcam, ab137869). After washing three times with PBS for 10 min, sections were incubated with the corresponding secondary antibodies (Alexa Fluor 594 donkey anti-mouse IgG, Thermo Fisher Scientific, USA; Alexa Fluor 594 donkey anti-rabbit IgG, Thermo Fisher Scientific, USA) for 1 h at room temperature. Sections were then stained with DAPI (Abcam, ab104139) for 10 min at room temperature. Images were acquired using a Zeiss confocal microscope and analyzed with ImageJ software.

After sorting, LSK cells were placed in 2% FBS-containing solution. For cytospin preparation, cells were counted and adjusted to 3 × 10^4 cells per slide in a final volume of 10 μL. The suspension was loaded into Thermo Scientific Cytospin 4 cytocentrifuge and spun onto standard adhesion glass slides at 1,000 rpm for 3 min, producing visible cell spots on the slides. Approximately 20 μL methanol was gently applied along the edge of the cell spot to avoid disturbing the cell monolayer. After methanol evaporation, the slides were air-dried and fixed. Slides were washed three times with PBS for 10 min and then permeabilized with 0.3% Triton X-100 in PBS for 30 min. After blocking with 5% donkey serum in PBS for 1 h, samples were incubated overnight at 4°C with primary antibodies (rabbit anti-mouse beta 2 Adrenergic Receptor Ab, Abcam, ab182136; rabbit anti-mouse beta 3 Adrenergic Receptor Ab, Abcam, ab94506). After washing three times with PBS for 10 min, sections were incubated with the corresponding secondary antibodies (Alexa Fluor 488 donkey anti-mouse IgG, Thermo Fisher Scientific, USA) for 1 h at room temperature. Cells were then stained with DAPI (Abcam, ab104139) for 10 min at room temperature. Images were acquired using a Zeiss confocal microscope and analyzed with ImageJ software.

Chemogenetic manipulation of PVN neurons in mice

To manipulate PVN neuronal activity, rAAV-hSyn-hM3D(Gq)-EGFP-WPRE-hGH polyA (excitatory DREADD) and rAAV-hSyn-hM4D(Gi)-EGFP-WPRE-hGH polyA (inhibitory DREADD) viruses were generated (BrainVTA). To selectively target CRH neurons, rAAV-CRH-hM3D(Gq)-mCherry-WPRE and rAAV-CRH-hM4D(Gi)-mCherry-WPRE viruses were constructed to activate or inhibit CRH-expressing neurons (BrainVTA), respectively. Neuronal targeting was verified by immunofluorescence. Mice were deeply anesthetized, and viral vectors were delivered by stereotactic intracranial injection into the PVN (coordinates relative to bregma: −0.7 mm posterior, ± 0.2 mm lateral, and −47 mm ventral). After injection, mice were allowed to recover for two weeks to ensure sufficient expression of DREADDs receptors in PVN neurons. For chemogenetic activation or inhibition, mice received intraperitoneal injections of clozapine-N-oxide (CNO, BrainVTA, 1 μg/g) twice daily, while control mice received an equal of 0.9% saline. Young mice were treated for 5 days, whereas aged mice were treated for 2 weeks.

Spatial transcriptomics of mouse brain after PRV tracing

Five days after PRV tracing from the femur, mice were perfused and brains were collected. Tissues were fixed in paraformaldehyde, dehydrated in a sucrose gradient, embedded in OCT, and frozen. Brain tissues were sectioned at 5 μm thickness using a Leica cryostat. During sectioning, slices were examined under a fluorescence microscope until a large number of symmetrical $EGFP^+$ neurons were observed in the PVN of the hypothalamus. Selected sections were mounted on DSP-specific slides. Each slide contained brain sections from six mice (three young and three aged) and was stored on dry ice for further processing. According to the DSP protocol, sections were subjected to antigen retrieval using a pressure cooker, followed by washing. Protein denaturation was performed to facilitate antibody labeling. Proteinase K digestion was applied to expose RNA targets. Samples were then fixed with formaldehyde at room temperature for 5 min. Sections were incubated overnight in the dark with a morphology marker antibody (eGFP) and probes from the Whole Transcriptome Atlas (WTA) panel. Nuclear staining was performed using SYTO13 according to the DSP protocol before imaging.

Tissue sections were imaged under a microscope, and regions of interest (ROIs) were selected. Collected oligonucleotides were transferred to a collection plate, sealed with a breathable membrane, and processed for library preparation. PCR amplification was performed following the DSP standard workflow. Libraries were prepared using magnetic beads, quantified using QFX, and fragment sizes were assessed using a Qsep100 system before sequencing according to the DSP protocol. Image data were segmented to identity nuclear and cytoplasmic regions. Background correction and spatial alignment were performed to remove non-specific signals and ensure accurate spatial mapping. After quality control and normalization, gene expression matrices were generated. Differentially expressed genes were visualized using heatmaps and volcano plots, and pathway enrichment analysis was performed to identify significantly enriched signaling pathways.

Flow cytometry

Single-cell suspensions from bone marrow or peripheral blood were prepared and incubated in FACS buffer (2% FBS and 5 mM EDTA). Cells were stained with indicated antibodies for 30 min at 4°C . The following antibodies were used for FACS: PE-Cy7 anti-CD5, BV785 anti-B220, BV711 anti-IgM, BV421 anti-IgD, FITC anti-CD43, PE anti- CD24, APC anti-BP-1, AF700 anti-CD3, AF700 anti-CD11b, AF700 anti-GR1, AF700 anti-Ter119, APC-CY7 anti-CD45, PE anti-CD19, FITC anti-CD23, APC anti-CD2, AF700 anti-Sca1, FITC anti-CD3, BV421 anti-NK1.1, AF647 anti-rabbit IgG, lin- mix(anti-mouse CD8 biotin, anti-mouse CD4 biotin, anti-mouse CD45R biotin, anti-mouse CD11b biotin, anti-mouse CD8Ter-119 biotin, anti-mouse Ly-6G biotin), APC-CY7 anti-mouse IgG, PE-CY7 anti-ckit, AF700 anti-SCA1, APC anti-CD16/32, PE anti-CD34, FITC anti-CD127, BV421 anti-CD150, BV711 anti-CD48, APC anti-CD69, PE anti-DNTT,APC anti-PAX5. Dead cells were excluded using 7-AAD (BioLegend) or Zombie (BioLegend). Flow cytometry data were acquired using FACSAria III cytometer (BD Biosciences) and analyzed with FACSDiva software (v8.0.2) and FlowJo (v10.0.7).

Fiber photometry recording of calcium signaling

To investigate the activity of CRH-PVN neurons in 3-month-old and 18-month-old mice, 300 nL of pAAV-CRH promoter-jGCaMP8s-WPRE (Shanghai Obio Technology) was stereotaxically injected into the PVN. An optical fiber was implanted 50 μm dorsal to the injection site. Fluorescence signals were acquired using a single-channel fiber photometry system (Thinker Tech). Recordings commenced with mice freely behaving in their home cage for 5 min to establish baseline activity. Subsequently, mice were gently transferred to a novel environment, a clean plastic cage (41 cm × 19 cm × 20.5 cm) for 5 min. After this exposure, mice were returned to their home cage for an additional 5 min of recording. The fiber-optic cable was then carefully detached from the head-mounted baseplate at the conclusion of data acquisition. Fluorescence changes were quantified as ΔF/F, where F represents the mean fluorescence intensity during the home-cage baseline period.

Transmission electron microscopy

Transmission Electron Microscopy (TEM) was used to determine the location of TLR4 in $EGFP^+$ cells within the PVN. Mice were deeply anesthetized and perfused intracardially with 1× PBS. A $1mm^3$ tissue block from the PVN was dissected and fixed in fixative solution (Servicebio, G1124-100ML). After washing three times with PBS, samples were dehydrated through a graded ethanol series, infiltrated with resin, and embedded in capsules. Polymerization was performed in a low-temperature ultraviolet polymerizer at -20°C for 48 h. Ultrathin sections (70 - 80 nm) were cut using an ultramicrotome and collected on coated nickel grids. Immunolabeling was performed before imaging with a transmission electron microscope. The following primary antibodies were used: rabbit anti-mouse TLR4 Ab (Abcam, ab22048) and rabbit anti-mouse EGFP Ab (Thermo Fisher, CAB4211).

Primary hypothalamic neuron culture

Hypothalamic neurons were isolated from E15.5-E16.5 mouse embryos. After isolation of hypothalamic under sterile condition, the tissue was carefully washed in wash buffer. The brain tissue was digested with papain digestion buffer (500 μL per brain) at 37°C for 30 min. Digestion was terminated by adding plating medium, and the cell suspension was passed through a cell strainer. The cell suspension was counted and seeded into poly-L-lysine-coated tissue culture plate. After 6 h, the medium was replaced with complete Neurobasal medium (48.5 mL Neurobasal medium, 1 mL B27 supplement, and 0.5 mL L-glutamate in a total volume of 50 mL). Half of the medium was replaced every 48 h. On day 7, the culture medium was switched to a glutamine-free formulation. Cells were maintained at 37°C in a humidified incubator with 5% CO_2. mRNA levels of *Tlr4, Ifng, Il1b*, and *Cxcl10* were measured by RT-qPCR on days 6, 14, and 21 of culture. Protein levels of TLR4, IFNγ, NF-κB, phosphorylated-NF-κB (pNF-κB), IκB, and phosphorylated-IκB (pIκB) were analyzed by western blot. Neuronal activation and senescence were assessed by immunofluorescence staining for c-Fos and β-galactosidase (β-gal), respectively.

Quantitative PCR with reverse transcription

Total RNA was extracted from cultured hypothalamic neurons using a TIANGEN RNA extraction kit (TIANGEN, DP420) and reverse-transcribed into cDNA using a Thermo Fisher reverse

transcription kit (Thermo Fisher, 11756050). Gene expression levels were measured by quantitative real-time polymerase chain reaction (RT-PCR) in triplicate on an ABI QuantStudio 5 Sequence Detection System (Thermo Fisher) using FastStart Universal SYBR Green Master (ROX) (Roche). Expression levels were normalized to GAPDH and calculated using the ΔΔCt method.

Western blotting analysis

Protein samples were isolated from cultured hypothalamic neurons using RIPA buffer (R0010, Solarbio). Proteins were denatured by boiling in 5 × SDS loading buffer separated by SDS–polyacrylamide gel electrophoresis, followed by transfer to polyvinylidene fluoride membrane. Membranes were blocked with 5% skim milk for 1 hour at room temperature and incubated overnight at 4°C with primary antibodies. The following primary antibodies were used: mouse TLR4 (Abcam, ab22048), rabbit IFNγ (proteintech, 15365-1-ap), rabbit NF-κB (CST, 8242S), rabbit P-NF-κB (CST, 303S), mouse IκB (CST, 8242S), rabbit P-IκB (CST, 2859S), rabbit β-actin (Abcam, ab8227). Horseradish peroxidase (HRP)–conjugated secondary antibodies, including goat HRP-goat anti-rabbit immunoglobulin G (Beijing Zhongshan Golden Bridge Biotechnology Co. Ltd, ZB-2304) and goat HRP-goat anti-mouse immunoglobulin G (Beijing Zhongshan Golden Bridge Biotechnology Co. Ltd, ZB-2305), were incubated with blot membrane at room temperature for 1 hour, followed by detecting with ECL Western Blotting Detection Reagent (Thermon Fisher, 32132).

Bone marrow denervation by transaction of femoral and sciatic nerves

Denervation of the femoral bone marrow was performed. An incision was made to expose the femoral nerve, and a 1-cm segment of the nerve was excised. The incision was then sutured and disinfected. Bone marrow cells were collected 14 days later for flow cytometry analysis.

Hematopoietic stem cells (HSCs) sorting

For BM hematopoietic stem cell isolation, rinsed the bone marrow cell cavities of mice were flushed to obtain single cell suspensions. Red blood cells were depleted using red blood cell lysis buffer (Solarbio, R1010) for 10 min at 4°C. Cells were incubated with fluorescent antibody conjugates and 7AAD (BioLegend, 420440) for dead cell exclusion, and analyzed using a flow cytometer (FACSAria III, BD Biosciences) equipped with FACSDiva software (BD Biosciences). The following antibodies were used to sort HSCs: fluorescent c-kit, SCA1, CD48, CD150, biotinylated lineage antibodies (CD11b, CD8a, Ter119, CD45R, CD4, Ly-6G) (BD eBioscience). Biotinylated antibodies were detected with fluorochrome conjugated streptavidin (BD eBioscience).

Bulk RNA sequencing

A total 5,000 sorted HSCs were used for bulk RNA sequencing and placed in 100 μL of lysis buffer, then stored at −80°C. A modified Smart-seq2 single-cell RNA-seq protocol was used for cDNA library construction[44]. First, cell samples of each group were lysed, and the released RNA was precipitated using 80% ethanol. Secondly, reverse transcription was performed by synthesizing the first strand using an oligo(dT) primer (5′-AAGCAGTGGTATCAACGCAGAGTACT30VN-3′) with

SuperScript II reverse transcriptase (Invitrogen, cat. no. 18064-014), followed by synthesis of a complementary strand using a template-switching oligo (5′-AAGCAGTGGTATCAACGCAGAGTACATrGrG+G-3′). For cDNA preamplification, an ISPCR primer (5′-AAGCAGTGGTATCAACGCAGAGT-3′) was used to amplify cDNA to the nanogram level. Finally, libraries were constructed using the TruePrep DNA Library Prep Kit V2 for Illumina (Vazyme, TD501/TD502/TD503) according to the manufacturer's instructions.

LSK cell sorting and culture

Bone marrow suspensions were aseptically obtained from the bilateral femurs of mice. Red blood cell lysis buffer was used to remove red blood cells, and the cells were then washed and prepared as single-cell suspensions at a concentration of 1 x 10^{7-8} cells/mL. Lin^- cells were isolated using a commercial kit (STEMCELL Technologies, 19856), and the enriched fraction was collected. Flow cytometric antibodies were used to sort LSK cells (PE-cy7 anti-ckit, FITC anti-Sca1). 7-AAD was used to exclude dead cells. Cells were sorted into sterile LSK culture medium using a FACSAria III cytometer. The culture medium consisted of SFEM (STEMCELL Technologies) supplemented with 100 ng/ml SCF, 100 ng/ml TPO, and tertiary antibody. Sorted cells were seeded in 24-well plates at a density of 1×10^5 cells/500 μL per well.

The sorted LSK cells were subjected to viral transfection. The multiplicity of infection (MOI) was set at 40, and the required amount of virus was calculated. Knockdown, overexpression, and control viruses were added separately. A total of 500 μL of virus, polybrene, and LSK medium was added to each well for resuspension. LSK cells were plated onto retronectin-coated 24-well plates and centrifuged at 2,000 rpm for 90 min. A second round of infection was performed the following day. Virus and polybrene were added again, followed by centrifugation at 2,000 rpm for 90 min. Cells were cultured at 37°C, in a humified incubator with 5% CO_2 for 10 h. The culture medium was then replaced to terminate the infection, and the cells were further cultured. Cells were collected 72 h after the initial transfection and analyzed using a FACSAria III cytometer.

After sorting, LSK cells were maintained in suspension culture. DMSO or propranolol was administered starting at 24 h, followed by DMSO or norepinephrine 1 h later. Norepinephrine was supplemented every 12 h, and propranolol every 24 h. Half of the medium was replaced after 48 h. After 72 h of norepinephrine treatment, the cells were collected and analyzed using a FACSAria III cytometer.

HA vaccine immunization

After chemogenetic intervention and CRH neuron specifical TLR4 knockdown, mice were immunized with an influenza vaccine. Each single-dose quadrivalent split influenza virus vaccine 500 μL, contained 15 μg of hemagglutinin from each viral strain including A/Michigan/45/2015 (H1N1) pdm09-like virus, A/Singapore/INFIMH-16-0019/2016 (H3N2)-like virus, B/Colorado/06/2017-like virus (B/Victoria/2/87 lineage), and B/Phuket/3073/2013 like virus (B/Yamagata/16/88 lineage). Mice were anesthetized with isoflurane, and the vaccine was administered intramuscularly into the thigh muscles (50 μL per mouse, corresponding to 15

hemagglutinin). Three weeks later, the same dose was administered as a booster to induce a secondary immune response.

Serum antibody analysis by ELISA

Serum samples for IgG measurement were collected from mice at day 14 and 28 after HA vaccination and diluted 1:50. ELISA was performed using a basic ELISA kit (MultiSciences Biotech). 96-well ELISA plates were coated with 2 mg/ml HA protein (Sino Biological, 40567-V08H1) in PBS overnight at 4°C. Diluted serum samples were then B l and incubated at 37°C for 1 h. After washing, the plate was further incubated with horseradish peroxidase (HRP)-conjugated goat anti-mouse total IgG (Sino Biological, 1:5,000) for 1 h, followed by development with TMB substrate. The reaction was stopped by adding 100 µL of 1 M H_2SO_4, and optical density (OD) was measured at 450 nm using a microplate reader.

Statistical analysis

Statistical analyses were performed using SPSS Statistics version 22 (IBM, Armonk, NY) and GraphPad Prism version 10.0 (GraphPad Software, La Jolla, CA). A two-tailed unpaired Student's t-test was used to compare data between two independent groups, while one-way analysis of variance (ANOVA) followed by Tukey's post hoc test was used for comparisons among three or more groups with a single variable. Two-way ANOVA was used to assess variation over time, followed by Tukey's post hoc test for multiple comparisons. The statistical significance of survival rates was evaluated using Kaplan-Meier survival curves and the log-rank test. A p-value < 0.05 was considered statistically significant. All experiments presented in this study were performed in duplicates. All data were presented as mean ± standard deviation (SD).

References

1 Chang, A. Y., Skirbekk, V. F., Tyrovolas, S., Kassebaum, N. J. & Dieleman, J. L. Measuring population ageing: an analysis of the Global Burden of Disease Study 2017. The Lancet. Public health 4, e159-e167, doi:10.1016/s2468-2667(19)30019-2 (2019).

2 Cunningham, A. L., McIntyre, P., Subbarao, K., Booy, R. & Levin, M. J. Vaccines for older adults. BMJ (Clinical research ed.) 372, n188, doi:10.1136/bmj.n188 (2021).

3 Jang, G. et al. Stem cell decoupling underlies impaired lymphoid development during aging. Proceedings of the National Academy of Sciences of the United States of America 120, e2302019120, doi:10.1073/pnas.2302019120 (2023).

4 Pardo-Seco, J. et al. High-Dose Influenza Vaccine to Reduce Hospitalizations. The New England journal of medicine 393, 2303-2312, doi:10.1056/NEJMoa2509834 (2025).

5 Liu, Z. et al. Immunosenescence: molecular mechanisms and diseases. Signal transduction and targeted therapy 8, 200, doi:10.1038/s41392-023-01451-2 (2023).

6 Terekhova, M. et al. Single-cell atlas of healthy human blood unveils age-related loss of NKG2C(+)GZMB(-)CD8(+) memory T cells and accumulation of type 2 memory T cells. Immunity 56, 2836-2854.e2839, doi:10.1016/j.immuni.2023.10.013 (2023).

7 Terekhova, M., Bohacova, P. & Artyomov, M. N. Human immune aging. Immunity 58, 2646-2669, doi:10.1016/j.immuni.2025.10.009 (2025).

8 Shi, F. D. & Yong, V. W. Neuroinflammation across neurological diseases. Science (New York, N.Y.) 388, eadx0043, doi:10.1126/science.adx0043 (2025).

9 Tracey, K. J. The inflammatory reflex. Nature 420, 853-859, doi:10.1038/nature01321 (2002).

10 Chavan, S. S., Pavlov, V. A. & Tracey, K. J. Mechanisms and Therapeutic Relevance of Neuro-immune Communication. Immunity 46, 927-942, doi:10.1016/j.immuni.2017.06.008 (2017).

11 Liu, Q. et al. Brain Ischemia Suppresses Immunity in the Periphery and Brain via Different Neurogenic Innervations. Immunity 46, 474-487, doi:10.1016/j.immuni.2017.02.015 (2017).

12 Kwan, W. et al. The Central Nervous System Regulates Embryonic HSPC Production via Stress-Responsive Glucocorticoid Receptor Signaling. Cell stem cell 19, 370-382, doi:10.1016/j.stem.2016.06.004 (2016).

13 Pierce, H. et al. Cholinergic Signals from the CNS Regulate G-CSF-Mediated HSC Mobilization from Bone Marrow via a Glucocorticoid Signaling Relay. Cell stem cell 20, 648-658.e644, doi:10.1016/j.stem.2017.01.002 (2017).

14 Janssen, H. et al. Monocytes re-enter the bone marrow during fasting and alter the host response to infection. Immunity 56, 783-796.e787, doi:10.1016/j.immuni.2023.01.024 (2023).

15 Ho, Y. H. et al. Remodeling of Bone Marrow Hematopoietic Stem Cell Niches Promotes Myeloid Cell Expansion during Premature or Physiological Aging. Cell stem cell 25, 407-418.e406, doi:10.1016/j.stem.2019.06.007 (2019).

16 Maryanovich, M. et al. Adrenergic nerve degeneration in bone marrow drives aging of the hematopoietic stem cell niche. Nature medicine 24, 782-791, doi:10.1038/s41591-018-0030-x (2018).

17 Gao, X. et al. Nociceptive nerves regulate haematopoietic stem cell mobilization. Nature 589, 591-596, doi:10.1038/s41586-020-03057-y (2021).

18 Zhang, X. et al. Brain control of humoral immune responses amenable to behavioural modulation. Nature 581, 204-208, doi:10.1038/s41586-020-2235-7 (2020).

19 Li, H. et al. Paraventricular nucleus CRH neurons regulate acute lung injury via sympathetic nerve-neutrophil axis. Nature communications 16, 8870, doi:10.1038/s41467-025-63953-7 (2025).

20 Jagot, F. et al. The parabrachial nucleus elicits a vigorous corticosterone feedback response to the pro-inflammatory cytokine IL-1β. Neuron 111, 2367-2382.e2366, doi:10.1016/j.neuron.2023.05.009 (2023).

21 Jiang, R. et al. Beta2 adrenergic receptor-mediated abnormal myelopoiesis drives neuroinflammation in aged patients with traumatic brain injury. Science advances 10, eadp5239, doi:10.1126/sciadv.adp5239 (2024).

22 Liu, W. et al. Traumatic brain injury stimulates sympathetic tone-mediated bone marrow myelopoiesis to favor fracture healing. Signal transduction and targeted therapy 8, 260, doi:10.1038/s41392-023-01457-w (2023).

23 Hofer, S. J., Rapp, S., Klenerman, P. & Simon, A. K. Understanding and improving vaccine efficacy in older adults. Nature aging 5, 1455-1470, doi:10.1038/s43587-025-00939-6 (2025).

24 Frasca, D. & Blomberg, B. B. B cell function and influenza vaccine responses in healthy aging and disease. Current opinion in immunology 29, 112-118, doi:10.1016/j.coi.2014.05.008 (2014).

25 Frasca, D., Diaz, A., Romero, M., Garcia, D. & Blomberg, B. B. B Cell Immunosenescence. Annual review of cell and developmental biology 36, 551-574, doi:10.1146/annurev-cellbio-011620-034148 (2020).

26 Gustafson, C. E., Kim, C., Weyand, C. M. & Goronzy, J. J. Influence of immune aging on vaccine responses. The Journal of allergy and clinical immunology 145, 1309-1321, doi:10.1016/j.jaci.2020.03.017 (2020).

27 Melo Dos Santos, L. S., Trombetta-Lima, M., Eggen, B. & Demaria, M. Cellular senescence in brain aging and neurodegeneration. Ageing research reviews 93, 102141, doi:10.1016/j.arr.2023.102141 (2024).

28 Morgan, J. I. & Curran, T. Stimulus-transcription coupling in neurons: role of cellular immediate-early genes. Trends in neurosciences 12, 459-462, doi:10.1016/0166-2236(89)90096-9 (1989).

29 Joo, J. Y., Schaukowitch, K., Farbiak, L., Kilaru, G. & Kim, T. K. Stimulus-specific combinatorial functionality of neuronal c-fos enhancers. Nature neuroscience 19, 75-83, doi:10.1038/nn.4170 (2016).

30 Doshi, P. P., Desale, S. H., Khutale, A. A., Sabarathinam, S. & Suresh, S. Evaluating Senescence-Targeted Approaches in Alzheimer's Disease: What We Know and What Lies Ahead. Ageing research reviews, 103029, doi:10.1016/j.arr.2026.103029 (2026).

31 Wu, D., Sun, J. K. & Chow, K. H. Neuronal cell cycle reentry events in the aging brain are more prevalent in neurodegeneration and lead to cellular senescence. PLoS biology 22, e3002559, doi:10.1371/journal.pbio.3002559 (2024).

32 Sangineto, M. et al. Metabolic reprogramming in inflammatory microglia indicates a potential way of targeting inflammation in Alzheimer's disease. Redox biology 66, 102846, doi:10.1016/j.redox.2023.102846 (2023).

33 Dou, R. X. et al. Aβ(1-42) promotes microglial activation and apoptosis in the progression of AD by binding to TLR4. Redox biology 78, 103428, doi:10.1016/j.redox.2024.103428 (2024).

34 Zhu, Z. et al. The S1P receptor 1 antagonist Ponesimod reduces TLR4-induced neuroinflammation and increases Aβ clearance in 5XFAD mice. EBioMedicine 94, 104713, doi:10.1016/j.ebiom.2023.104713 (2023).

35 Swaab, D. F. Ageing of the human hypothalamus. Hormone research 43, 8-11, doi:10.1159/000184230 (1995).

36 Hofman, M. A. Lifespan changes in the human hypothalamus. Experimental gerontology 32, 559-575, doi:10.1016/s0531-5565(96)00162-3 (1997).

37 Swaab, D. F., Bao, A. M. & Lucassen, P. J. The stress system in the human brain in depression and neurodegeneration. Ageing research reviews 4, 141-194, doi:10.1016/j.arr.2005.03.003 (2005).

38 Zhang, G. et al. Hypothalamic programming of systemic ageing involving IKK-β, NF-κB and GnRH. Nature 497, 211-216, doi:10.1038/nature12143 (2013).

39 Mather, M. & Nga, L. Age differences in thalamic low-frequency fluctuations. Neuroreport 24, 349-353, doi:10.1097/WNR.0b013e32835f6784 (2013).

40 Klein, F. et al. Dntt expression reveals developmental hierarchy and lineage specification of hematopoietic progenitors. Nature immunology 23, 505-517, doi:10.1038/s41590-022-01167-5 (2022).

41 Fedl, A. S. et al. Transcriptional function of E2A, Ebf1, Pax5, Ikaros and Aiolos analyzed by in vivo acute protein degradation in early B cell development. Nature immunology 25, 1663-1677, doi:10.1038/s41590-024-01933-7 (2024).

42 Labrie, J. E., 3rd, Borghesi, L. & Gerstein, R. M. Bone marrow microenvironmental changes in aged mice compromise V(D)J recombinase activity and B cell generation. Seminars in immunology 17, 347-355, doi:10.1016/j.smim.2005.05.012 (2005).

43 Yang, C. et al. Single-cell transcriptomics identifies premature aging features of TERC-deficient mouse brain and bone marrow. GeroScience 44, 2139-2155, doi:10.1007/s11357-022-00578-4 (2022).

44 Amoah, A. et al. Aging of human hematopoietic stem cells is linked to changes in Cdc42 activity. Haematologica 107, 393-402, doi:10.3324/haematol.2020.269670 (2022).

Supplementary Files

This is a list of supplementary files associated with this preprint. Click to download.

- 3DviewofPRVEGFPlabeledPVNneuronsin3montholdmice.mp4
- 3DviewofPRVEGFPlabeledPVNneuronsin18montholdmice.mp4